Bioactive Materials 25 (2023) 239–255

Contents lists available at ScienceDirect

Bioactive Materials

journal homepage: www.keaipublishing.com/en/journals/bioactive-materials

Biomineralization inspired 3D printed bioactive glass nanocomposite scaffolds orchestrate diabetic bone regeneration by remodeling micromilieu

Zeqian Xu [a,b,c,d,e,f,1], Xuanyu Qi [a,b,c,d,e,f,1], Minyue Bao [a,b,c,d,e,f], Tian Zhou [d,g], Junfeng Shi [a,b,c,d,e,f], Zhiyan Xu [h], Mingliang Zhou [a,b,c,d,e,f], Aldo R. Boccaccini [h], Kai Zheng [i,j,*], Xinquan Jiang [a,b,c,d,e,f,**]

[a] Department of Prosthodontics, Shanghai Ninth People's Hospital, Shanghai Jiao Tong University School of Medicine, No. 639 Zhizaoju Road, Shanghai, 200011, People's Republic of China
[b] College of Stomatology, Shanghai Jiao Tong University, No. 639 Zhizaoju Road, Shanghai, 200011, People's Republic of China
[c] National Center for Stomatology, No. 639 Zhizaoju Road, Shanghai, 200011, People's Republic of China
[d] National Clinical Research Center for Oral Diseases, No. 639 Zhizaoju Road, Shanghai, 200011, People's Republic of China
[e] Shanghai Key Laboratory of Stomatology, No. 639 Zhizaoju Road, Shanghai, 200011, People's Republic of China
[f] Shanghai Engineering Research Center of Advanced Dental Technology and Materials, No. 639 Zhizaoju Road, Shanghai, 200011, People's Republic of China
[g] Department of Oral Maxillofacial-Head and Neck Oncology, Shanghai Ninth People's Hospital, College of Stomatology, Shanghai Jiao Tong University School of Medicine, Shanghai, 200023, People's Republic of China
[h] Institute of Biomaterials, University of Erlangen-Nuremberg, Cauerstrasse 6, 91058, Erlangen, Germany
[i] Jiangsu Province Engineering Research Center of Stomatological Translational Medicine, Nanjing Medical University, Nanjing, 210029, People's Republic of China
[j] Jiangsu Key Laboratory of Oral Diseases, Nanjing Medical University, Nanjing, 210029, People's Republic of China

ARTICLE INFO

Keywords:
Biomineralization
Type II Diabetes mellitus
3D printing
Sr-containing mesoporous bioactive glass nanoparticles
Enzymatic cross-links

ABSTRACT

Type II diabetes mellitus (TIIDM) remains a challenging clinical issue for both dentists and orthopedists. By virtue of persistent hyperglycemia and altered host metabolism, the pathologic diabetic micromilieu with chronic inflammation, advanced glycation end products accumulation, and attenuated biomineralization severely impairs bone regeneration efficiency. Aiming to "remodel" the pathologic diabetic micromilieu, we 3D-printed bioscaffolds composed of Sr-containing mesoporous bioactive glass nanoparticles (Sr-MBGNs) and gelatin methacrylate (GelMA). Sr-MBGNs act as a biomineralization precursor embedded in the GelMA-simulated extracellular matrix and release Sr, Ca, and Si ions enhancing osteogenic, angiogenic, and immunomodulatory properties. In addition to angiogenic and anti-inflammatory outcomes, this innovative design reveals that the nanocomposites can modulate extracellular matrix reconstruction and simulate biomineralization by activating lysyl oxidase to form healthy enzymatic crosslinked collagen, promoting cell focal adhesion, modulating osteoblast differentiation, and boosting the release of OCN, the noncollagenous proteins (intrafibrillar mineralization dependent), and thus orchestrating osteogenesis through the Kindlin-2/PTH1R/OCN axis. This 3D-printed bioscaffold provides a multifunctional biomineralization-inspired system that remodels the "barren" diabetic microenvironment and sheds light on the new bone regeneration approaches for TIIDM.

1. Introduction

Diabetes mellitus (DM), a chronic, systemic metabolic disease and characterized by hyperglycemia due to deficient or dysfunctional insulin sensitivity, will reach an alarming global prevalence of almost 10.9% (700 million people) by 2045 [1]. With the characteristics of insulin

Peer review under responsibility of KeAi Communications Co., Ltd.
* Corresponding author. Jiangsu Province Engineering Research Center of Stomatological Translational Medicine, Nanjing Medical University, Nanjing, 210029, People's Republic of China.
** Corresponding author. Department of Prosthodontics, Shanghai Ninth People's Hospital, Shanghai JiaoTong University School of Medicine, No. 639 Zhizaoju Road, Shanghai, 200011, People's Republic of China.
E-mail addresses: kaizheng@njmu.edu.cn (K. Zheng), xinquanjiang@aliyun.com (X. Jiang).
[1] These authors contributed equally to this work.

https://doi.org/10.1016/j.bioactmat.2023.01.024
Received 9 October 2022; Received in revised form 10 January 2023; Accepted 30 January 2023

resistance and high prevalence, type II diabetes mellitus (TIIDM) is mostly suffered by middle-aged and elderly people and is accompanied by jeopardized function and complications of multiple tissues, thus severely threatening the quality of life of the patient [2,3].

As a consequence of alterations in the host metabolism, persistent hyperglycemia contributes to the accumulation of advanced glycation end products (AGEs) and leads to stimulation of reactive oxygen species (ROS) and escalated production of the inflammasomeNACHT-LRR-PYD domain-containing protein 3 (NLRP3) and proinflammatory cytokines (IL-1β), thus inducing chronic inflammation accompanied by increased proinflammatory M1 macrophage polarization and diminished anti-inflammatory M2 macrophage polarization [4–6]. As a result, inflammation reduces the capillary formation and induces endothelial dysfunction, contributing to microvascular disease and impaired bone healing [7,8].

Hyperglycemia and a constant inflammatory state could directly impinge on bone metabolism, biomineralization, and the osteogenesis process [7,9]. The serum levels of osteocalcin (OCN) are decreased in DM, which alters calcium and phosphate homeostasis [10]. Additionally, the impairment of parathyroid hormone activity is also observed in DM, which could further induce disordered phosphorus and calcium (Ca–P) metabolism [11,12]. This disordered Ca–P metabolism further results in the alteration of osteo-differentiation into adipo-differentiation and impairs osteogenic differentiation, which inhibits bone regeneration and reduces bone quality and quantity [4,7,9,13]. The collagenous matrix , which is the basis for bone mineralization, features increased glycation-induced crosslinking and shows brittle mechanical properties in the diabetic microenvironment. This may further decrease bone quality in terms of poor biomineralization, increased bone fracture risks [14–16], and impaired bone healing [2,17].

Clinically, the rising number of diabetic patients remains a massive challenge for the medical specialties of dentistry and orthopedics, where the numerous procedures involving bone replacement or augmentation are impacted by delayed and/or impaired bone regeneration, thus compromising clinical outcomes and increasing clinical failures [2,15,18–20]. Hyperglycemia, infection, chronic inflammation, reduced angiogenesis, impaired osteogenesis, and granulation tissue formation are challenges of diabetic wound healing and bone regeneration [21–25].

Till now, various biomaterials loaded with bioactive components (growth factors, extracellular vesicles [EVs], etc.) have been utilized for diabetic bone regeneration. Anti-inflammation, angiogenesis, and osteogenesis are the targets for tissue regeneration in type II diabetes mellitus (TIIDM) [22,25]. To improve the impaired angiogenesis, small extracellular vesicles targeting endothelial cells immobilized on polymeric coating for β-TCP scaffolds were carried out [26]. To reverse the proinflammatory micro-environment, 3D-printed GelMA scaffolds containing mesoporous silica nanoparticles (MSNs) loaded with BMP-4 were constructed for accelerating diabetic bone regeneration [27]. However, during the application, there exist great uncertainty about the dysfunction of those unstable bioactive components in the microenvironment. In addition, concerning the imbalanced Ca and P metabolism and impaired bone mineralization in diabetic micromilieu, the concept of modulation of diabetic biomineralization has not been fully addressed so far.

Targeting “remodeling” of the pathologic diabetic micromilieu, the development of bioinspired materials that modulate bone regeneration via biomimetic mineralization could be an innovative strategy. Sr plays important role in the modulation of bone metabolism for osteoporosis [28], glucose regulation for TIIDM [29], and enhance proliferation and osteogenic differentiation of mesenchymal stem cells [30]. In this work, we selectedSr-containing mesoporous bioactive glass nanoparticles (Sr-MBGNs) based on the impressive osteogenic, angiogenic, immunomodulatory, and biomineralization-prone activities of Sr, Ca, and Si ions, which could also act as the biomineralization precursors embedded in the extracellular matrix (constructed with gelatin methacrylate, GelMA, EFL, China) to modulate the dynamic process of biomineralization [31,32]. Launching a combination of biomimetic materials with 3D printing, which can mimic the highly organized and complex hierarchical structure of natural hard tissue [33], sheds new light on the potential for bone regeneration in diabetic patients [34].

2. Results and discussion

2.1. Materials characterization of Sr-MBGNs incorporated 3D-printed scaffold

In this study, we used Sr-MBGNs with different Sr concentrations as rigid fillers to enhance the mechanical properties, mineralization, and biological performance of 3D-printed hydrogel scaffolds. SEM images show the sphere-like shape of Sr-MBGNs, and TEM images confirm their mesoporous structure (diameter approximately 150 nm) (Fig. 1a). The results indicated that Sr incorporation did not significantly affect the mesoporous structure or sphere-like shape when both Ca and Sr were included in the MBGNs. However, when CaO was completely substituted with SrO (30Sr-MBGNs), the resulting nanoparticles exhibited a larger particle size larger than that of other Sr-MBGNs. In addition, the outer surface of 30Sr-MBGNs appeared to be covered by a thin coating that was likely a Sr-rich phase (Fig. 1a). However, Sr-MBGNs remained amorphous regardless of the Sr concentration, as evidenced by the XRD results (Fig. S1a), which ensured the biodegradability of these nanoparticles.

Mesoporous bioactive glass nanoparticles (MBGNs) are characterized by their mesoporous structure with large specific surface area and superior surface reactivity [32], which was confirmed by using the nitrogen sorption analysis. As shown in Fig. S1b, the results indicate a typical isotherm of mesoporous materials [35,36]. The presence of Sr in the particles did not significantly influence the pore size and SSA for 0Sr-, 5Sr, and 15Sr-MBGNs, except for 30Sr-MBGNs showing increased pore size and decreased specific surface areas (SSA).

In addition, the biological performances (e.g., osteogenic, angiogenic, and immunomodulatory activities) of MBGNs can be tailored by the incorporation of biologically active ions [31,37]. We used GelMA as the printable ink to print hydrogel scaffolds considering the superior biocompatibility and printability.

As indicated by the ICP results, all scaffolds exhibited a continuous release of Si ions over 14 d (Fig. 1 b), suggesting the degradation of Sr-MBGNs. As expected, 30Sr, 15Sr, and 5Sr-MBGNs released Sr ions in a sustained way. However, 30Sr-MBGNs could release significantly larger amounts of Sr ions than 15Sr and 5Sr-MBGNs, probably due to the presence of a Sr-rich layer on 30Sr-MBGNs (Fig. 1 a). The Ca ion-releasing curve showed a constant decreasing trend. Omit the existing Ca concentration in the high glucose DMEM, as shown in Fig. 1 b, the decrease of Ca ions could be attributed to the consumption of Ca during the mineralization (HA formation) process of 0Sr-MBGNs, 5Sr-MBGNs, and 15Sr-MBGNs group after exposure to high glucose DMEM, which will be discussed below [38]. Few hydroxyapatite (HA) formations in 30Sr-MBGNs and no HA formation in GelMA might contribute to an overall constant unchanged level of Ca releasing.

The SEM of the freeze-dried 3D-printed scaffolds showed a regular printing structure (Fig. 1 c). The optical images of the scaffolds after incubation in DMEM for 14 d show that the pure GelMA scaffolds could not retain their stable porous structure after 14 d in the culture medium, whereas other Sr-MBGNs-containing scaffolds still exhibited porous structures. Notably, we observed some mineral deposition in the 0Sr-, 5Sr-, and 15Sr-MBGNs scaffolds, which could be the formed calcium phosphate species (CaP). In addition, it was observed that the hydrogels turned whitish after incubation in DMEM (high glucose) for 14 d, probably due to the deposition of calcium phosphate species. SEM images (Fig. 1d) show the deposition of Needle-like nanostructures on 0Sr-, 5Sr-, and 15Sr-scaffolds, which are likely the formation of HA crystals

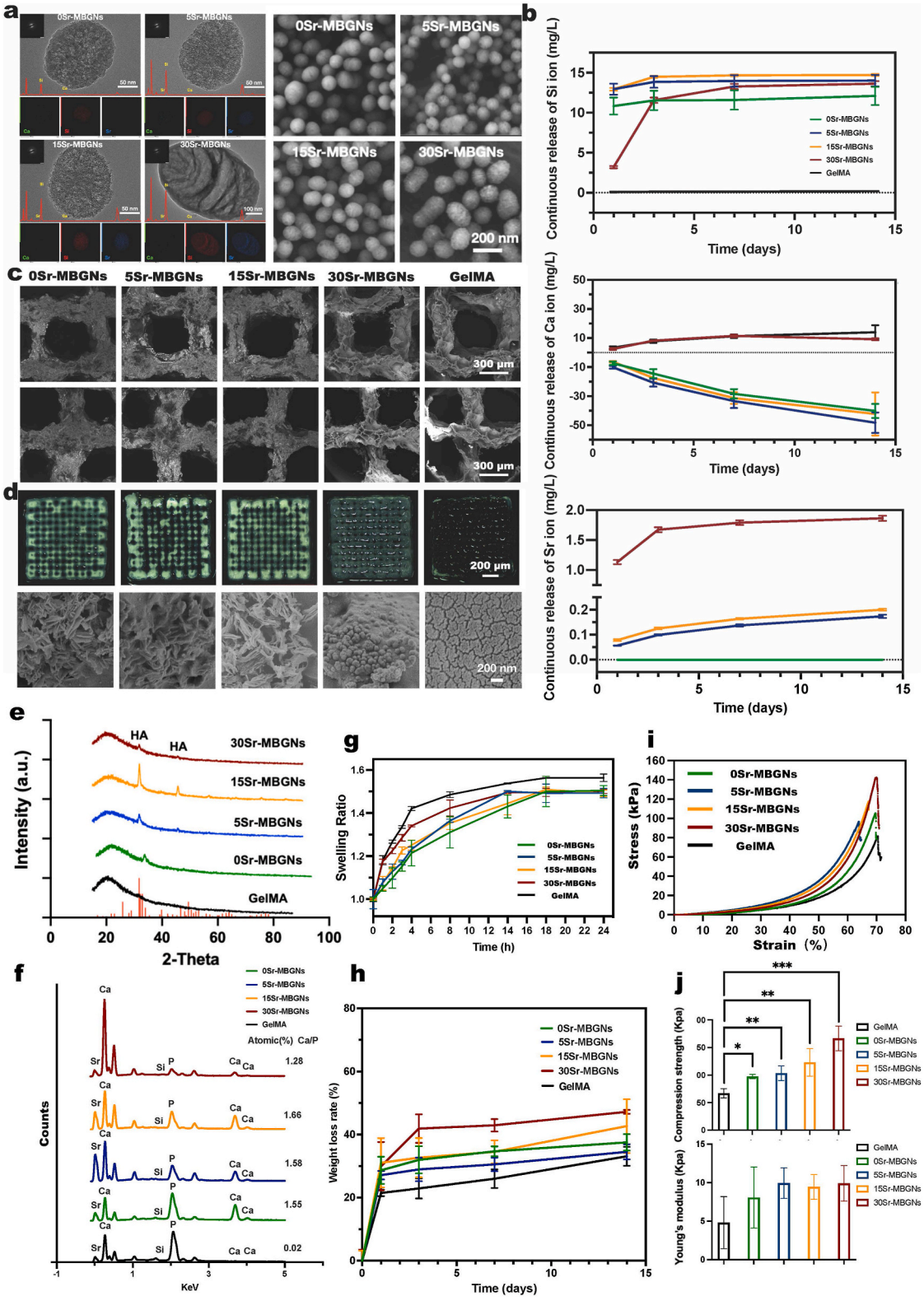

Fig. 1. Characterization of Sr-MBGNs and Sr-MBGNs incorporated 3D-printed scaffolds. a) TEM and SEM characterization of Sr-MBGNs; b) ICP characterization of the Sr, Ca, and Si ions released by the 3D-printed scaffolds at 1 d, 3 d 7 d, and 14 d after incubation in high glucose DMEM; c) SEM characterization of the 3D-printed GelMA hydrogel scaffolds incorporated with Sr-MBGNS; d) Mineralization of scaffolds after incubation with DMEM (high glucose) for 14 days and the formation of CaP and HA as observed in the transaction region by SEM; e) XRD patterns confirmation of the formation of CaP and HA during the mineralization process (scaffold incubate in SBF for 14d); f) EDS analysis of the formation of CaP and HA during SEM analysis of the mineralization on the scaffold; g) Swelling behaviors of the 3D-printed hydrogel scaffolds; h) degradation behavior of the 3D-printed hydrogel scaffolds; i) Compression stress-strain curve of the scaffolds; j) Compression strength and Young's modulus of the scaffolds.

[39]. Instead, spherical nanostructures were observed on the scaffold of the 30Sr-MBGNs group which might be the formation of amorphous calcium phosphate (ACP) [39], while only the cracked surface was observed on pure GelMA scaffolds after dissolution in simulated body fluid (SBF) [40]. Energy dispersive spectroscopy (EDS) and X-ray diffraction (XRD) results (Fig. 1 e, f) confirmed the formation of calcium phosphate species on the Sr-MBGNs containing scaffolds after immersion in SBF as the presence of P was detected. As a comparison, P could not be detected on the surface of GelMA scaffolds, indicating the absence of calcium phosphate-based species including HA and amorphous calcium phosphate. For the EDS outcome, the Ca/P ratio of HA normally ranges from 1.5 to 1.67, which is in accordance with the Ca/P of 0Sr-MBGNs, 5Sr-MBGNs, and 15Sr-MBGNs Groups (Fig. 1 f). The Ca/P of amorphous calcium phosphate (ACP) ranges from 1.2 to 2.2, which might indicate the ACP existence in the 30Sr-MBGNs group [41]. XRD results (Fig. 1 e) confirmed the formation of hydroxyapatite (HA) crystals. The diffraction peaks could be observed on XRD patterns of the freeze-dried scaffolds of 0Sr-MBGNs, 5Sr-MBGNs, and 15Sr-MBGNs group. The peaks located at 33° and 48° can be attributed to HA crystals (ICDD No. 9–432) according to the ICDD database [42]. Tiny diffraction peaks could be observed on the XRD pattern of the 30Sr-MBGNs group, which suggested that HA also formed in the 30Sr-MBGNs group, but the amount was low. No diffraction peaks could be observed on the XRD pattern of GelMA scaffolds, which was consistent with the results of SEM and EDS.

In summary, the results indicate that the incorporation of Sr-MBGNs, as biomineralization precursors, significantly enhanced the HA formatting ability of GelMA scaffolds (promoting mineralization). The 30Sr-MBGNs group appeared to have lower in vitro mineralization compared to other Sr-MBGNs, probably due to the lack of Ca in their compositions. It is known that Ca plays a key role in calcium phosphate formation [39].

An increase in the swelling ratio weakens the mechanical properties of hydrogels [43], in our case incorporation of Sr-MBGNs could decrease the swelling ratio and increase mechanical properties (compression strength and Young's modulus) (Fig. 1 g,h). In this nanocomposite system, Sr-MBGNs acted as a precursor of mineralization and bridged GelMA molecules, which improved the integration of the scaffolds, and consequently enhanced the mechanical performances of GelMA scaffolds (Fig. 1 I,j) [44]. The incorporation of 0Sr-MBGNs, 5Sr-MBGNs, and 15Sr-MBGNs didn't significantly influence the degradation of the GelMA scaffolds (Fig. 1 h), which might be due to the balance between degradation and the formation of HA [45,46]. However, few HA formations (Fig. 1 d, e, f) and higher ion release (Fig. 1b) in 30Sr-MBGNs scaffolds might result in more significant weight loss. Moreover, to simulate the clinical situation, the analysis of the mechanical properties and degradation of the scaffolds in a blood/saliva environment at a biological temperature of 37 °C. in future studies are necessary. Studies focus on modulating the distribution of nanoparticles, the channels tailored by 3D printing, and interactions between fillers and matrices to optimize the degradation of composites so that they could coordinate the speed of tissue in-growth with materials degradation are highly recommended in the future [47,48].

2.2. Osteogenic function and stimulated biomineralization of Sr-MBGNs-incorporated 3D-printed scaffolds

2.2.1. Optimization of Sr-MBGNs concentrations

BMSCs harvested from type II diabetic rats (TIID BMSCs) and cultured in DMEM (high glucose+500 ng/ml lipopolysaccharide (LPS)) were used here to simulate the type II diabetic model in vitro. The extraction solutions from 10 mg/ml, 5 mg/ml, 1 mg/ml, and 0.1 mg/ml 0Sr-MBGNs, 5Sr-MBGNs, 15Sr-MBGNs, and 30Sr-MBGNs were incubated with TIID BMSCs for 24 h to evaluate the cytotoxicity and screen the optimized concentration. The concentrations of 1 mg/ml and 0.1 mg/ml showed great biocompatibility (Fig. S2 a). Given that the hydrogel could retard the ion release from Sr-MBNGs, therefore, 1 mg/ml Sr-MBGNs were finally chosen to be dispersed in GelMA for further application as the raw material for 3D printing. An enhanced promotion effect especially for 15Sr- and 30Sr-MBNs scaffolds was observed when TIID BMSCs were incubated with and seed on the 3D-printed scaffolds (Fig. S2 b, c). ALP and ARS staining outcome of TIID BMSCs cultured with 3D-printed scaffolds showed that the 15 Sr-MBGNs and 30Sr-MBGNs group exhibited superior osteogenic effects (Fig. S2 d). The osteogenesis-related gene expression level of ALP, Runx2, OCN, COL-1, and Osterix were significantly elevated, particularly for the 15Sr-MBGNs and 30Sr-MBGNs groups after 7 d of incubation with TIID BMSCs (Fig. S2 e). These results confirmed the promoted proliferation and osteogenic differentiation induced by Sr ion [28,30].

2.2.2. In vivo characterization of the osteogenic function

As shown in Fig. 2 a,b, the microCT data, HE, and Masson staining outcomes indicated satisfactory osteogenesis outcomes for the Sr-MBGNs groups. The Sr-MBGNs-incorporated scaffolds boosted bone regeneration by establishing a biomineralization stimulating, ion-rich, thus regeneration-friendly microenvironment.

2.2.2.1. Bioinspired-biomineralization promoted osteogenesis. The application of polymer-based hydrogels for bone regeneration is always accompanied by limited mineralization (HA layer formation), which can influence effective bonding with bone tissues and bone ingrowth. Bioactive glass is a type of material with an active rapid biomineralization function when exposed to simulated body fluid (SBF). Here, dispersing Sr-MBGNs mesoporous bioactive glass nanoparticles (as CaP biomineralization precursor) in GelMA (as the extracellular matrix) aims to form a bionic bone regeneration microenvironment to initiate the bionic biomineralization process.

As proven by microCT, HE and Masson staining outcomes (Fig. 2 a, b), the 15Sr-MBGNs and 30Sr-MBGNs groups exhibited superior and accelerated bone regeneration at the 4 w and 8 w post-implantation compared to those of the GelMA and control groups in the diabetic rat model. Regarding bone microarchitectural morphology, improved trabecular connectivity and decreased porosity were observed, indicating improved bone quality. In addition, the bone growth rate was significantly promoted in the 15 and 30Sr-MBGNs groups, as indicated by sequential fluorescence (Fig. 2 c). The underlying mechanism for biomineralization and bone formation in diabetic rats was further investigated below.

Regarding natural bone biomineralization, the following three parts play quite essential roles in the entire process (Fig. 3): 1) prenucleation ion permeation (calcium $Ca^{2+}$and inorganic phosphate Pi), 2) collagen-rich extracellular matrix (ECM), and 3) noncollagenous proteins (NCPs) [49]. According to the new nonclassical biomineralization theory, there are two major processes: 1) sequestration of calcium and phosphorous ions into fluidic amorphous calcium phosphate (ACP) precursors and 2) templating these clusters into regular forms, which is modulated by extracellular noncollagenous proteins (NCPs) and other biomolecules [50,51]. These processes contribute to the intrafibrillar and extrafibrillar mineralization of collagen. Subsequently, the mineralized fibrils are further bundled into a highly ordered and stacked structure, forming either compact or spongy bone (Fig. 4 a) [52].

1) Sr-MBGNs-incorporated scaffolds regulate the ion prenucleation

As reported, mineral homeostasis and osteoid production are significantly decreased in TIIDM patients [12], which might represent a new target for improving bone quality in patients. Will the scaffold-produced ionic environment modulate the biomineralization process by regulating ion metabolism?

As shown in the gene ontology (GO) enrichment of ion metabolism (Fig. S3), the calcium ion homeostasis and the regulation of the

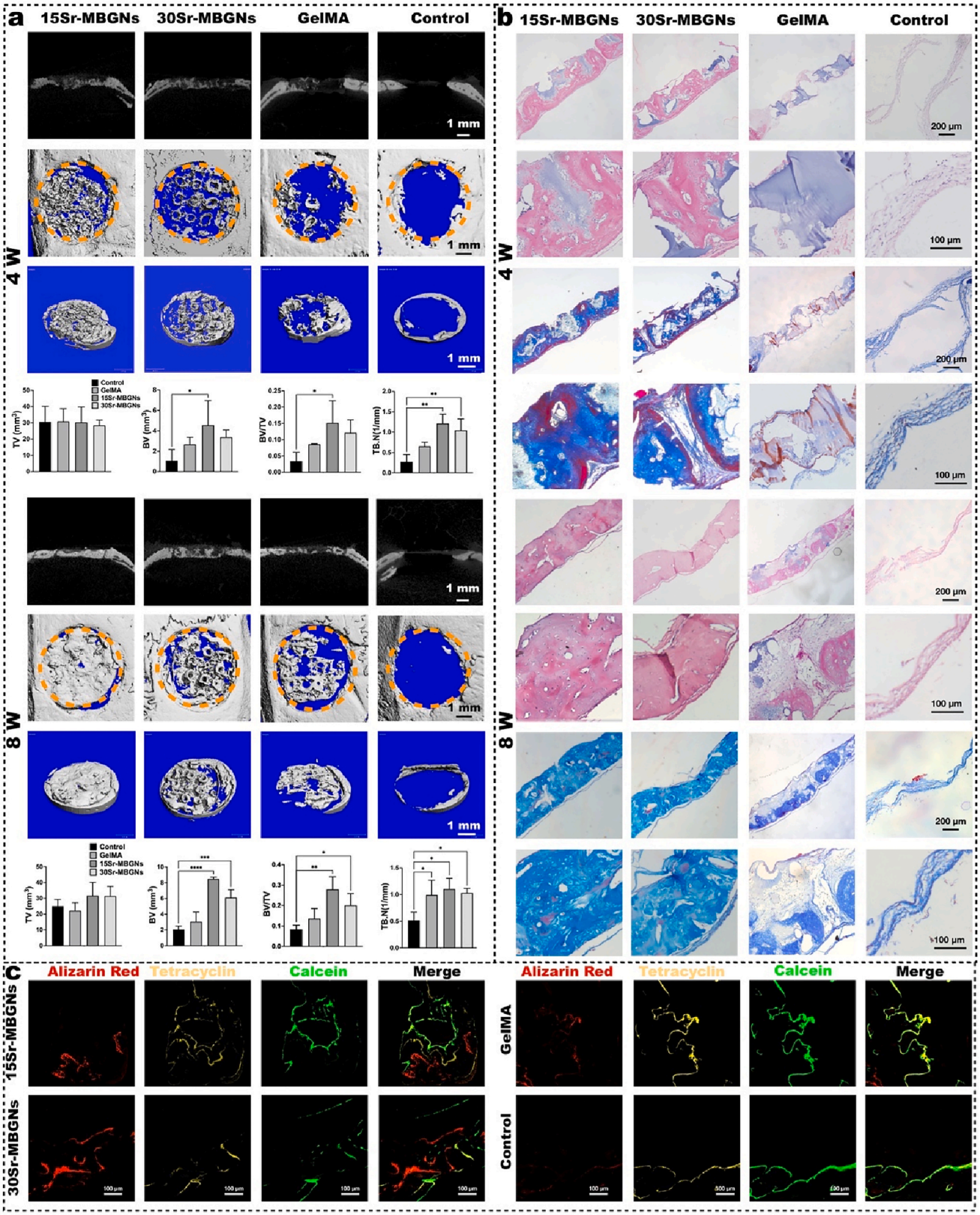

Fig. 2. Bone regeneration was enhanced by Sr-MBGNs scaffolds in a type II diabetic rat critical cranial bone defect model. a) Representative 2D/3D micro-CT images and quantitative analysis of samples harvested at 4 weeks (w) and 8 weeks (w) after implantation. ($^{*}p < 0.05$, $^{**}p < 0.01$,$^{***}p < 0.001$,$^{****}p < 0.0001$) b) H&E and Masson trichrome staining of the decalcified sections. c) Sequential fluorescence labeling shows that significant calcium deposition at 14 d (Alizarin Red), 28 d (Tetracycline), and 42 d (Calcein) is accompanied by bone growth in the defect region of the 15Sr-MBGNs and 30Sr-MBGNs groups compared with those of the control and GelMA groups.

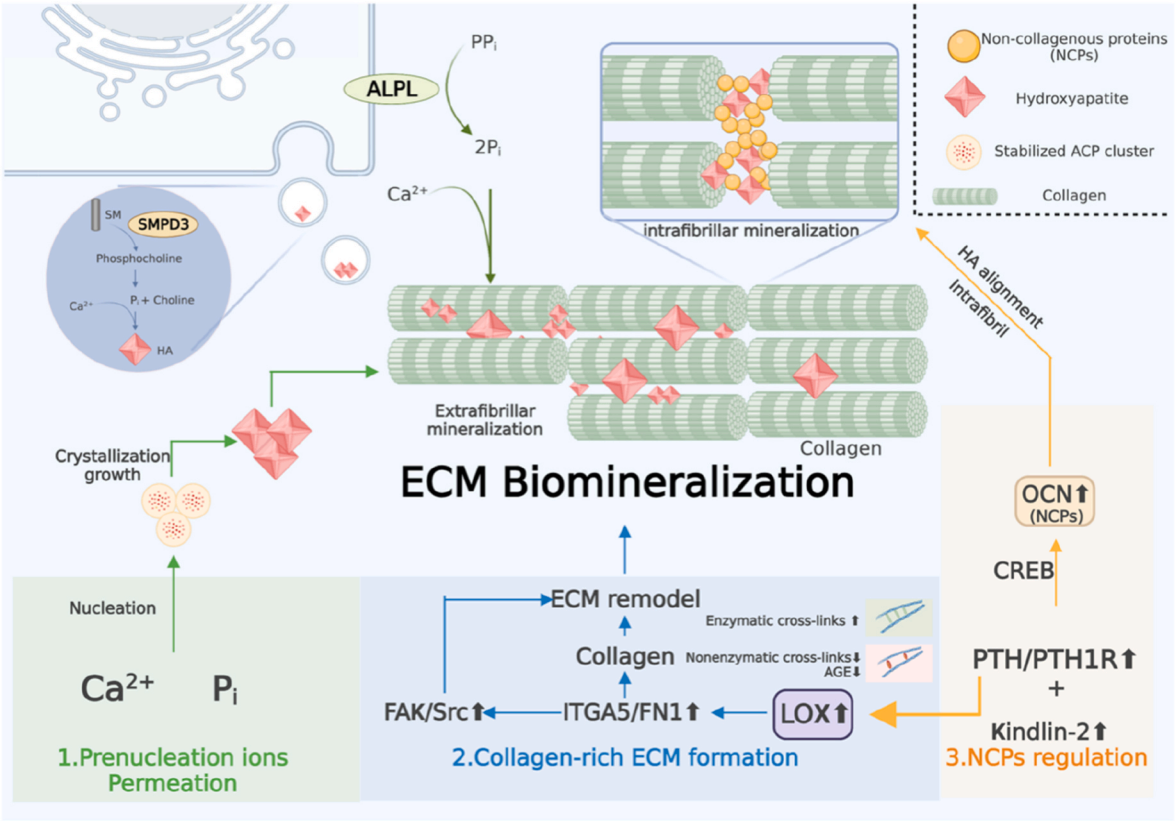

Fig. 3. Schematic description of the bioinspired biomineralization modulation mechanism of the 3D-printed Sr-MBGNs-incorporated scaffolds. The scaffolds biomimetically modulate the intrafibrillar and extrafibrillar biomineralization process by: 1) regulating the prenucleation ion aggregation and permeation; 2) upregulating LOX, thus promoting the enzymatic crosslinks and ECM reconstruction to form collagen-rich ECM; 3) promoting cell focal adhesion by upregulation of Kindlin-2, which could further activate the PTH1R and stimulate the excretion of OCN (a type of NCPs) to regulate the intrafibrillar HA alignment and intrafibrillar mineralization (schematic was created with BioRender.com).

phosphate metabolic process were promoted by the Sr-MBGNs scaffolds, particularly for the 15Sr-MBGNs group (4 weeks), which might be due to the consistent leaching out of Sr, Ca, Si ions playing an important role in modulating Ca and P homeostasis. The GO enrichment of biomineralization at 4 w (Fig. S4), indicated that both the 15Sr-MBGNs and 30Sr-MBGNs groups exhibited significantly activated biomineralization and bone mineralization.

The underlying mechanism might depend on alkaline phosphatase (ALPL), an ectoenzyme on the surface of the osteoblast membrane, which was elevated by the Sr-MBGNs-containing scaffolds (Fig. S2 d), ALPL can cleave inorganic pyrophosphate (PPi, a potent mineralization inhibitor) and promote the generation of the activator of ECM mineralization Pi (inorganic phosphate). The alteration of the Pi/PPi ratio in the bone regeneration microenvironment thus further promotes bone mineralization [49,52]. In addition, matrix vesicle (MV)–mediated mineralization acts as an auxiliary mechanism for bone mineralization. MV transfers the intracellular mineralization-promoting enzymes such as SMPD3, which was promoted by 15Sr- and 30Sr-MBGNs-containing scaffolds (Figs. 3 and 5), liberating free Pi and precipitating with Ca^{2+} and thus contributing to the formation of nascent HA [49].

2) Sr-MBGNs-incorporated scaffolds modulate the formation of collagen-rich ECM

Type I collagen plays a determining role in bone formation. Consequently, the formation of collagen-rich extracellular matrix (ECM) and appropriate mineralization deposition on the ECM is considered an important decisive factor for bone mineralization [50]. In terms of the deposition patterns of HA in collagen, the biomineralization of type I collagen includes intrafibrillar mineralization (HA deposits within the gap zone of collagen fibrils) and extrafibrillar mineralization (HA distribution on the surfaces of collagen fibrils) [51].

In such circumstances, a compact hierarchical assembly of collagen molecules in the fibrils and fibers contributes to both intra- and interfibrillar nanoscale gaps that are particularly essential for intrafibrillar mineralization, because these gaps are only accessible by small molecules such as Ca^{2+} and Pi ions, but not by the large protein inhibitors of ECM mineralization [49,51].

Stabilization and assembly of newly formed collagen fibers are primarily achieved by covalent intermolecular crosslinking between neighboring collagen molecules, which comprises enzymatic crosslinking (lysyl oxidase [LOX]-mediated crosslinking) and non-enzymatic cross-linking (glycation- or oxidation-induced AGE crosslinking forming AGEs) (Fig. 4 a). In the healthy physiological process, the total amount of enzymatic crosslinking in bone, which determines further bone mineralization and mechanical properties, is strictly regulated by the expression of LOX [53]. For type II diabetes, the switch from enzymatic to nonenzymatic crosslinking contributes to excess accumulation of collagen-AGEs, thus attenuating bone quality and raising bone fracture susceptibility (Fig. 4 a) [53,54]. Additionally, AGEs could further inhibit osteoblast differentiation and downregulate the expression level of LOX, thereby inducing the formation of brittle collagen fibers with an accumulation of microdamage, causing bone collagen degradation and further hindering the biomineralization process, which ultimately contributes to a positive feedback cycle [14,55–57].

Interestingly, our bionic biomineralization 3D-printed scaffolds could subtly interfere with such a cycle by targeting LOX. As shown in the RNA sequencing results, at the 4 w, the LOX gene was upregulated in

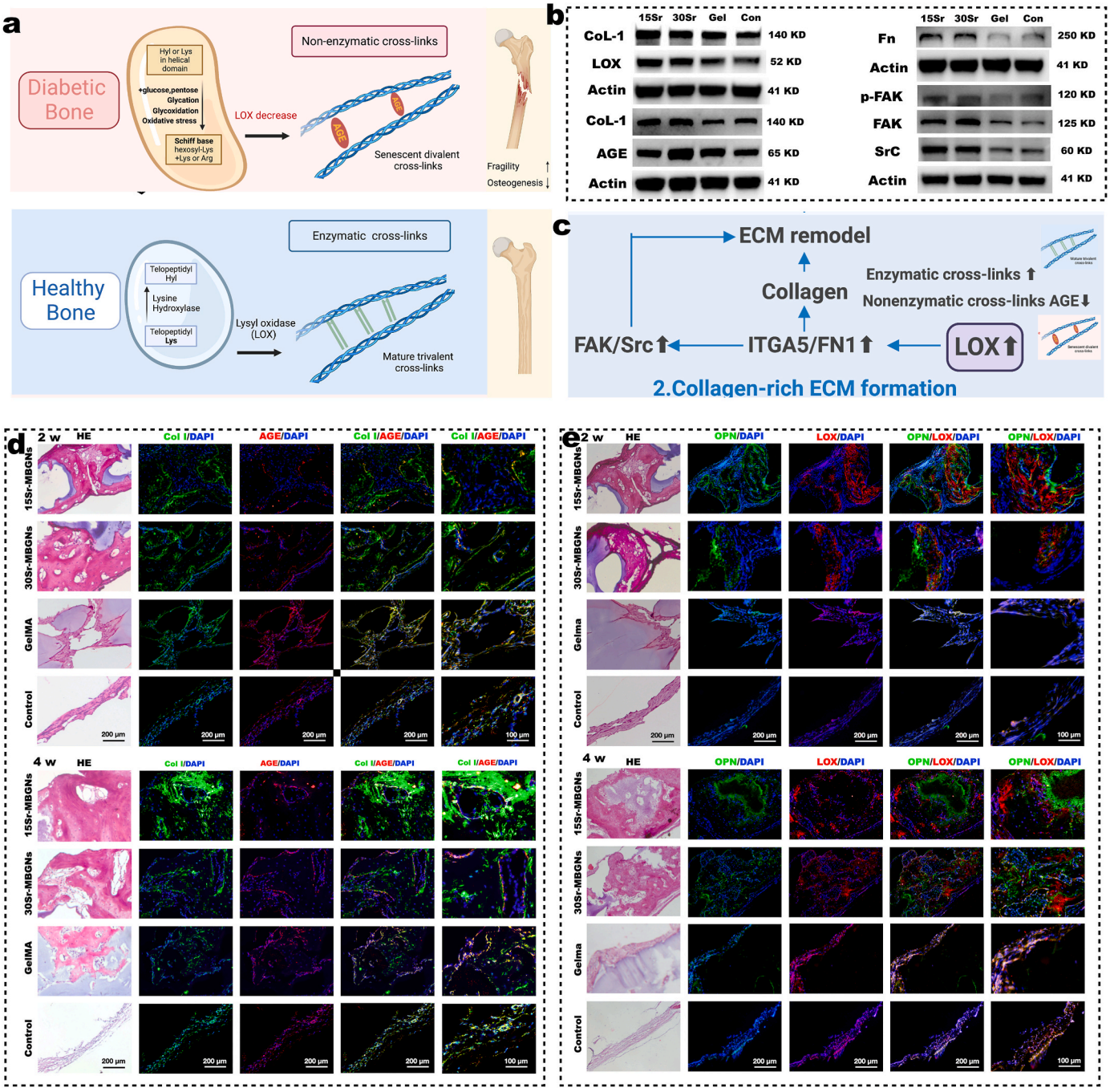

Fig. 4. The collagen crosslink modulation effect of Sr-MBGNs scaffolds depends on upregulating the LOX/ITGA5/FN/FAK/Src axis. a) Schematic of the mechanism behind collagen crosslink-regulation (schematic created with BioRender.com). b) Representative Western blot analysis. c) Schematic of the critical pathway of collagen-rich ECM formation. d-e) Representative H&E and immunofluorescence staining, respectively, in decalcified samples harvested at 2 w and 4 w after implantation.

the diabetic bone defect region in the 15Sr-MBGNs and 30Sr-MBGNs groups (Fig. 5 c). As verified by WB (Fig. 4 b), the expression levels of LOX, Fn, FAK, p-FAK, and Src in TIID BMSCs incubated with 15 and 30Sr-MBGNs scaffolds for 7 d were elevated, which indicates that the scaffolds promoted collagen crosslinking, fibronectin assembly, cell adhesion, and ECM remodeling functions through the LOX/ITGA5/FN FAK/Src signal axis (Fig.4 c, Figs. S5 and S6) [58]. FAK and Src play important role in governing intracellular signals mediating integrin function and the osteogenetic cell adhesion to ECM or biomaterials [59]. Sr^{2+} could promote the adhesion and proliferation of cells on biomaterials [60]. Cytoskeleton rearrangement is required to drive morphological changes in cells during adhesion and differentiation processes, as well as to guide the release of calcification vesicles into the ECM [61]. Importantly, Src has also been related to governing ECM remodeling by somehow contributing to matrix metalloproteinase (MMP) involvement in response to biomaterials.

The upregulated LOX could boost the expression of type I collagen (CoL-1) [62], which was proven by the WB results (Fig. 4 b). Additionally, when comparing the AGE/CoL-1 ratio in the WB results (Fig. 4 b), the 15Sr-MBGNs group in particular was lower than those of the control and GelMA groups, which indicates that the upregulated LOX promoted the expression of CoL-1 and promoted the enzymatic

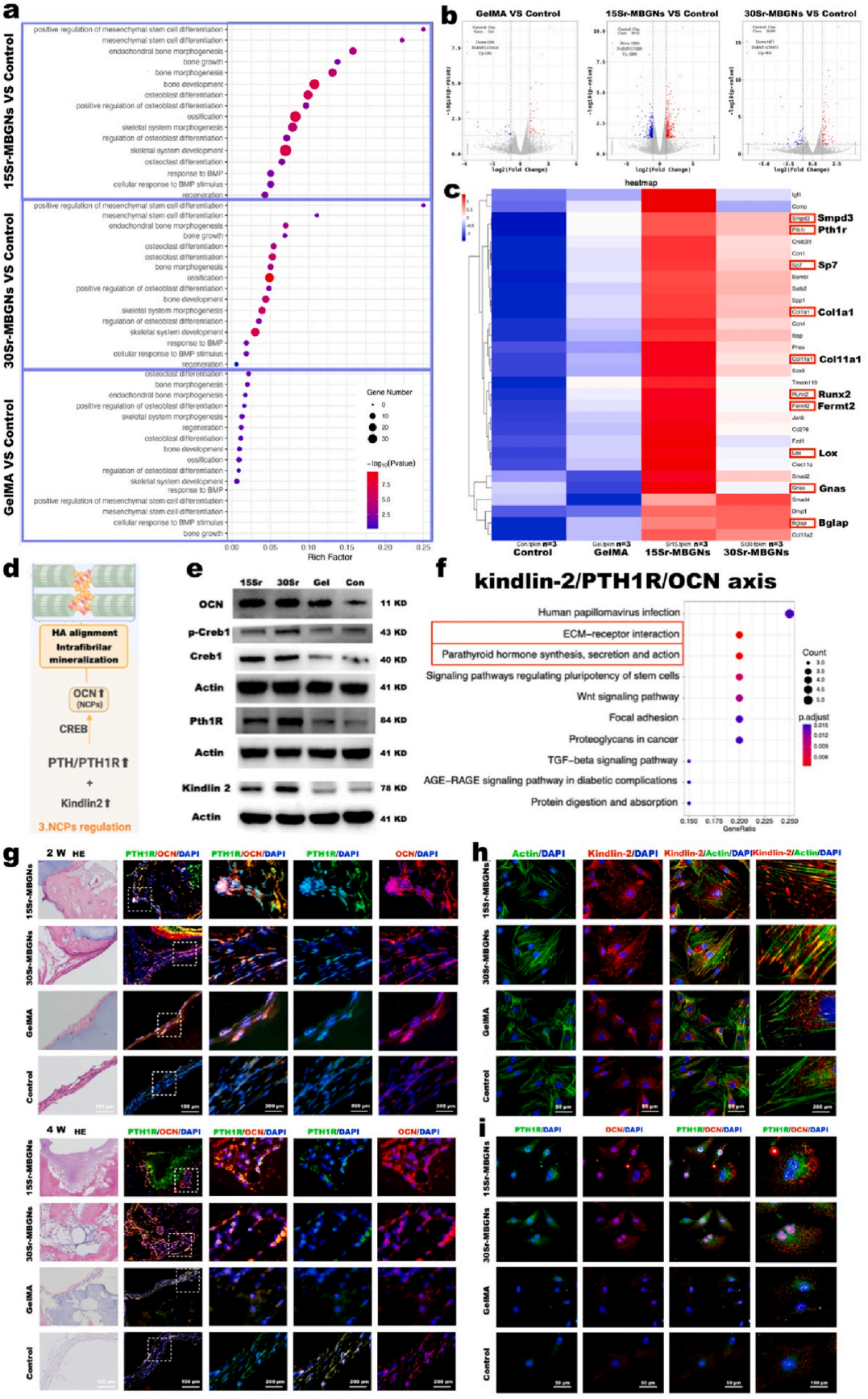

(caption on next page)

Fig. 5. Osteogenesis enhancement induced by Sr-MBGNs scaffolds promoted NCPs secretion and Kindlin-2/PTH1R/OCN axis upregulation. a) GO enrichment analysis of osteogenesis function; b) Volcano plots indicating the differentially expressed upregulated and downregulated genes for Sr-MBGNs and GelMA group; c) The related upregulated genes collected from the GO enrichment of osteogenesis function presented in the heatmap; d) Schematic of the NCPs regulation mechanism (schematic created with BioRender.com); e) Representative Western blot analysis verifying the upregulation of the Kindlin-2/PTH1R/OCN axis at the protein level; f) KEGG pathway analysis screening the most correlated signaling pathways; g) IHC indicating the positive correlation between the expression level of OCN and PTH1R at 2 w and 4 w with HE staining used to display the bone defect region; h) immunofluorescent staining confirming the high expression level of Kindlin-2 in TIID BMSCs after 7 d incubation with 15Sr and 30Sr-MBGNs groups; i) immunofluorescent staining indicating the positive correlation between OCN and PTH1R for TIID BMSCs after 7 d incubation with the scaffolds.

crosslink, overwhelming the nonenzymatic crosslink in the diabetic microenvironment, and therefore promoting biomineralization. As shown in the immunofluorescent images, the CoL-1-positive areas (Fig. 4 d) in the 2 w and 4w bone defect regions for the 15Sr- and 30Sr-MBGNs groups were superior to the GelMA and the control groups. The trend of the AGE-positive area is contrary to that of CoL-1 (Fig. 4 d). In Fig. 4 e, the LOX-positive areas in the 15Sr- and 30Sr-MBGNs groups at 2 and 4 w, were positively correlated with the osteogenesis protein OPN and significantly higher than those in the GelMA and control groups. Taken together, the Sr-MBGNs 3D-printed bioscaffolds could mimic the biomineralization process by working on the target LOX, promoting the enzymatic crosslinking of CoL-1 and constructing an environment conducive to bone mineralization and osteogenesis.

3) Sr-MBGNs-incorporated scaffolds promote the expression of NCPs

As mentioned above, extracellular noncollagenous proteins (NCPs) play an important role in modulating intrafibrillar mineralization by regulating the sequestration of Ca and Pi into fluidic amorphous calcium phosphate (ACP) precursors and templating HA nanocrystal deposits in the gap zone of collagen fibrils into ordered oriented forms [49,63].

OCN is known as one of the most abundant noncollagenous proteins (NCPs) in bone tissue, orchestrating bone matrix mineralization and systematic metabolism. OCN is characteristically expressed by osteoblasts and can attach to collagen, regulating the infiltration of CaP nanoclusters into fibrils and adjusting the alignment of HA nanocrystals, thus forming intrafibrillar mineralization; therefore, OCN was considered key to the alignment of apatite crystallites during mineralization [63].

Regardless, for type II diabetes, a high-glucose environment, and insulin resistance could induce downregulated OCN levels [64], because the differentiation of osteoblasts was suppressed by high glucose levels and decreased OCN serum concentrations [10].

Surprisingly, in the diabetic bone defect model, favorable osteogenesis effects could still be obtained by the Sr-MBGNs scaffolds in this barren diabetic microenvironment. As observed in the GO enrichment analysis, mesenchymal stem cell differentiation, bone growth, bone morphogenesis, osteoblast differentiation, and ossification were promoted in the 15Sr- and 30Sr-MBGNs groups (Fig. 5 a,b,c). In addition, the elevated expressions of PTH1R, LOX, Sp7 (osterix), Col1a1, Runx2, Fermt2 (kindlin-2), and Bglap (OCN) could be observed in the heatmap (Fig. 5 c). We propose that ions (Ca, Sr, and Si) leached out from Sr-MBGNs could modulate the excretion level of OCN from osteoblasts , working as NCPs and thus further regulating the biomineralization process (Fig. 5 d, e).

What is the underlying mechanism for this phenomenon? As displayed in the KEGG analysis, the pathways related to ECM-receptor interaction and parathyroid hormone synthesis, secretion and action were activated (Fig. 5 f).

For vertebrates, the type 1 parathyroid hormone receptor (PTH1R) is a critical regulator of mineral ion homeostasis (calcium/phosphate homeostasis), skeletal development, and bone regeneration, which can be activated by parathyroid hormone (PTH) and parathyroid hormone-related protein (PTHrP) [65,66]. PTH1R stimulation could promote mesenchymal stem cell (MSC) differentiation into osteoblasts and subsequent osteoblast proliferation and differentiation while inhibiting osteoblast apoptosis [67].

Kindlin-2 functions as an intrinsic component of the PTH1R signaling pathway for osteoblasts regulating the balance of bone mass and homeostasis. The interplay and cooperation between Kindlin-2 and PTH1R are essential for regulating bone homeostasis [65]. Kindlin-2, as a key focal adhesion protein, plays an important role in activating integrin and promoting cell-extracellular matrix (ECM) adhesion and migration [68]. Loss of Kindlin-2 inhibits RhoA activation and reduces focal adhesion assembly [69]. Additionally, adipogenesis of MSC differentiation, which is common in the diabetic micromilieu could be altered by Kindlin-2 and be switched into osteogenesis direction [69].

As shown in the gene expression heatmap, both Kindlin-2 (fermt2) and PTH1R were significantly upregulated in the 15Sr- and 30Sr-MBGNs groups (Fig. 5 c). The downstream OCN (Bglap) level was also significantly elevated (Fig. 5 c). Based on the KEGG analysis, we propose that kindlin-2/PTH1R/OCN is the main pathway here (Fig. 5 d). This hypothesis was verified by the WB results (Fig. 5 e), which showed increased Kindlin-2, PTH1R, and OCN levels in TIID BMSCs after 7d of incubation with the 15Sr-MBGNs and 30Sr-MBGNs-incorporated scaffolds. When incubating the TIID BMSCs with the 3D-printed scaffolds, a significantly increased Kindlin-2 fluorescence signal was observed in the 15Sr- and 30Sr-MBGNs groups (Fig. 5 h), in addition, the increased expression of PTH1R was positively correlated with OCN for the 15Sr- and 30Sr-MBGNs group (Fig. 5 i). This elevated expression level of PTH1R and OCN was also proven in the 2 w and 4 w immunofluorescent staining of the cranial defect tissue, showing a positive correlation between the OCN-positive and PTH1R-positive areas (Fig. 5 g).

In summary, Kindlin-2 and PTH1R promote ion homeostasis and reverse the low expression level of OCN (one type of important NCPs) in the diabetic micromilieu, working together with the PTH1R downstream LOX [55] and thus playing an essential role in modulating biomineralization and osteogenesis in diabetic bone defects [70,71].

The human body is full of multiphase biomaterials, as nearly every tissue contains, at a minimum, cells, a fibrous protein, and a biopolymer matrix [72]. Simulating the natural biomineralization process and searching for pathogenic targeting points, the combination of advancements in biomaterials, and advances in manufacturing provide new insights for further medical material design and manufacturing.

2.2.2.2. Immune modulation and diminished chronic inflammation. A low-inflammatory condition is considered essential to an osteogenesis-friendly environment.

In type II diabetes, a high glucose environment and advanced glycation end products (AGEs) stimulate the production of ROS, and the production is NADPH oxidase 2 (NOX-2) dependent. NOX-2 induces the production of ROS, and the intracellular ROS further stimulates downstream NACHT-LRR-PYD domain-containing protein 3 (NLRP3) and activates the pro-caspase-1 into caspase-1, thereby contributing to the increase in IL-1β secretion, further skewing wound macrophage polarization toward M1 macrophages and contributing to the chronic tissue inflammation [5,73,74]. Consistently, serum levels of proinflammatory cytokines such as TNFα and IL-1β are significantly elevated, indicating latent inflammation in type II diabetic (TIID) patients [4,75]. Inflammation is the first response of the immune system to infection or tissue injury. In diabetes, the NLRP3 inflammasome makes a significant contribution to the disease development and its complications such as osteoporosis and impairment of osteogenesis and wound healing [5,6]. Hence, the NOX-2/ROS/NLRP3/IL-1β axis plays an important role in the

immune imbalance of type II diabetes.

To investigate the immune modulation function, the 3D-printed scaffolds were directly cultured with TIID BMSCs in DMEM (high glucose+500 ng/ml LPS) to simulate the TIID diabetic micromilieu in vitro. The mitochondrial ROS level was significantly diminished in the 15Sr- and 30Sr-MBGNs groups compared with those of the GelMA and the control groups (Fig. 6 b). This is consistent with the weaker expression level of NLRP3 in TIID BMSCs when exposed to 15Sr- and 30Sr-MBGNs groups in the immunofluorescence staining images (Fig. 6 b) and the similar expression trend in tissue levels (Fig. 6 d). As shown in the WB results, the TIID BMSCs incubated in a high glucose and LPS environment for 24 h showed an increase in NOX-2, an elevated expression level of the NLRP3 inflammasome, and activation of caspase-1. The active caspase-1 further mediated the overproduction of IL-1β in the control and GelMA groups compared with the lower expression level in the 15Sr-MBGNs and 30Sr-MBGNs groups (Fig. 6 a, c). Thereafter, the downstream secretion of IL-1β could continuously mediate the polarization of macrophages and the severity of inflammation , which was evaluated through a coculture experiment of Raw 264.7 and the 3D-printed scaffolds in a simulated diabetic environment (DMEM high glucose + LPS).

As shown in the flow cytometry scatter and peak plot (Fig. 6 g, h), Raw 264.7 cells incubated with the 15Sr-MBGNs and 30Sr-MBGNs groups exhibited less M1 polarization (as detected with biomarker CD86) and more M2 polarization (as detected with biomarker CD206) than those of the control group. The tSNE analysis intuitively indicated the proportion of M1 polarization and M2 polarization intuitively (Fig. 6 g). As confirmed by immunofluorescence staining, the15Sr-MBGNs and 30Sr-MBGNs groups showed relatively stronger expression of CD206 and lower expression of iNOS than those of the control group (Fig. 6 e). This was also proven by the PCR results, in which the TNF-α and IL-1β were expressed at significantly lower levels in the 15Sr-MBGNs and 30Sr-MBGNs than those in the control group (Fig. 6 f). In summary, the 3D-printed bioscaffolds containing 15Sr-MBGNs and 30Sr-MBGNs displayed a predominant immune modulation function, which regulates the chronic inflammation in type II diabetes through the NOX-2/ROS/NLRP3/IL-1β axis, therefore furnishing an anti-inflammatory microenvironment for further cell recruitment, wound healing, and tissue regeneration such as bone ingrowth.

In addition, as an important focal adhesion protein, Kindlin-2, which works as the activator of PTH1R in the biomineralization process and was significantly upregulated by the 3D-printed scaffold (Fig. 6 c, e), also plays a critical role in inhibiting NLRP3 inflammasome activation, thus modulating inflammation [76].

2.2.2.3. Focal adhesion promoted vascularization-osteogenesis. In addition to biomineralization stimulation, a sufficient nutrient supply providing a fertile environment via angiogenesis is also essential for osteogenesis. For type II diabetic patients, the vascular endothelium is threatened by ROS, AGEs, and chronic inflammation resulting in dysfunction and depletion of the circulating endothelial progenitor cells (EPCs) and endothelial cells (ECs) [77], which play important roles in vascular repair and neovascularization. Thus, diabetic patients experience reduced angiogenic cytokines, reduced EPCs and ECs populations, and reduced recruitment due to their impaired cell proliferation, differentiation, adhesion mobilization, and migration [8,77].

4 w after the cranial bone defect, the healing process in the region of the 15Sr-MBGNs and 30Sr-MBGNs groups showed ascendant angiogenesis. As shown in the RNA sequence results, angiogenesis-related genes such as Vegfa, Vegfc, and Kdr were significantly upregulated in the 15Sr-MBGNs and 30Sr-MBGNs groups (Fig. 7 a), and the GO enrichment indicated that blood vessel development and morphogenesis, vasculature development, tube morphogenesis, and tube development were significantly activated in the 15Sr-MBGNs and 30Sr-MBGNs groups compared with those of the GelMA group (Fig. 7 b). The KEGG pathway analysis illustrated that the main correlated pathways were the PI3K-Akt signaling pathway and the focal adhesion pathway (Fig. 7 d).

In the focal adhesion pathway, focal adhesion kinase (FAK) plays an important role in angiogenesis by regulating ECs migration and invasion, which are highly correlated with PI3K and integral to the process of angiogenesis. Activated FAK can further form a complex with Src family kinases through the FAK/Src axis, which plays an essential role in VEGF-stimulated angiogenesis [78]. To explore the evidence supporting the GO and KEGG results, immunofluorescence staining was performed. As shown in Fig. 7 f, FAK expression in HUVECs was elevated in the 15Sr-MBGNs and 30Sr-MBGNs groups compared with those of the GelMA and the control groups. Consistently, at 2 w and 4 w, both the FAK-positive area and CD31-positive area in the 15Sr-MBGNs and 30Sr-MBGNs groups were significantly higher than those in the GelMA and control groups (Fig. 7 c), which indicated a positive correlation between FAK and the representative angiogenesis biomarker CD31 (Fig. 7 c).

Clinically, angiogenesis is crucial for promoting impaired wound healing in type II diabetic patients [17]. In addition, the bone blood vessel endothelium plays an essential role in bone mineralization and can tailor the process of bone remodeling and regeneration by delivering nutrients, oxygen, hormones, or growth factors [79]. Angiogenesis and osteogenesis are coupled mechanisms during bone development and healing. This may illustrate the correlation between the impairment of vascularization and high bone fragility in diabetic patients. At 4 w, the CD31-positive area was positively correlated with the Osterix-positive area, and both of them exhibited a relatively high expression level in the 15Sr-MBGNs and 30Sr-MBGNs groups (Fig. 7 e), which proves the vascularization-osteogenesis function of the scaffolds in TIID DM.

3. Conclusions

To transform the deleterious and barren diabetic micromilieu, Sr-MBGNs were dispersed in GelMA to construct biomineralized 3D-printed scaffolds. The Sr-MBGNs functioned as biomineralization precursors inducing the sequential formation of hydroxyapatite. We first revealed the interesting potential underlying osteogenic mechanisms of Sr-MBGNs nanocomposites, which promoted the formation of the pro-biomineralization environment through 1) modulation of ion homeostasis; 2) renovation of the diabetic pathologic nonenzymatic crosslink (AGEs) and promotion of the formation of LOX-mediated healthy enzymatic crosslinked collagen, thus facilitating ECM reconstruction; and 3) elevation of OCN (NCPs) levels to modulate the HA alignment of intrafibrillar mineralization through the Kindlin-2/PTH1R/OCN axis and further boost osteoblast differentiation. In addition, the bioactive scaffolds promoted angiogenesis and modulated chronic inflammatory conditions through the NOX-2/ROS/NLRP3/IL-1β axis, thus establishing a “fertile” bone regeneration microenvironment for TIID. In summary, our study provides a multifunctional biomineralization-inspired working unit promoting biomineralization, inhibiting inflammation, and accelerating vascularization to construct a “friendly” microenvironment for diabetic bone regeneration.

4. Experimental section

4.1. Material characterization

4.1.1. Synthesis of Sr-containing mesoporous bioactive glass nanoparticles

Sr-containing mesoporous bioactive glass nanoparticles (Sr-MBGNs) with various Sr concentrations were synthesized using a microemulsion-based sol-gel method as described in the literature [80]. In a typical process, 5.6 g of cetrimonium bromide (CTAB) was dissolved in 264 mL of deionized water under continuous stirring. Next, 80 mL of ethyl acetate (EA) was added when the CTAB was fully dissolved. After stirring for 30 min, 56 mL of aqueous ammonia (1 M) was added and followed by 15 min of stirring. Then, 28.8 mL of tetraethyl orthosilicate (TEOS) was

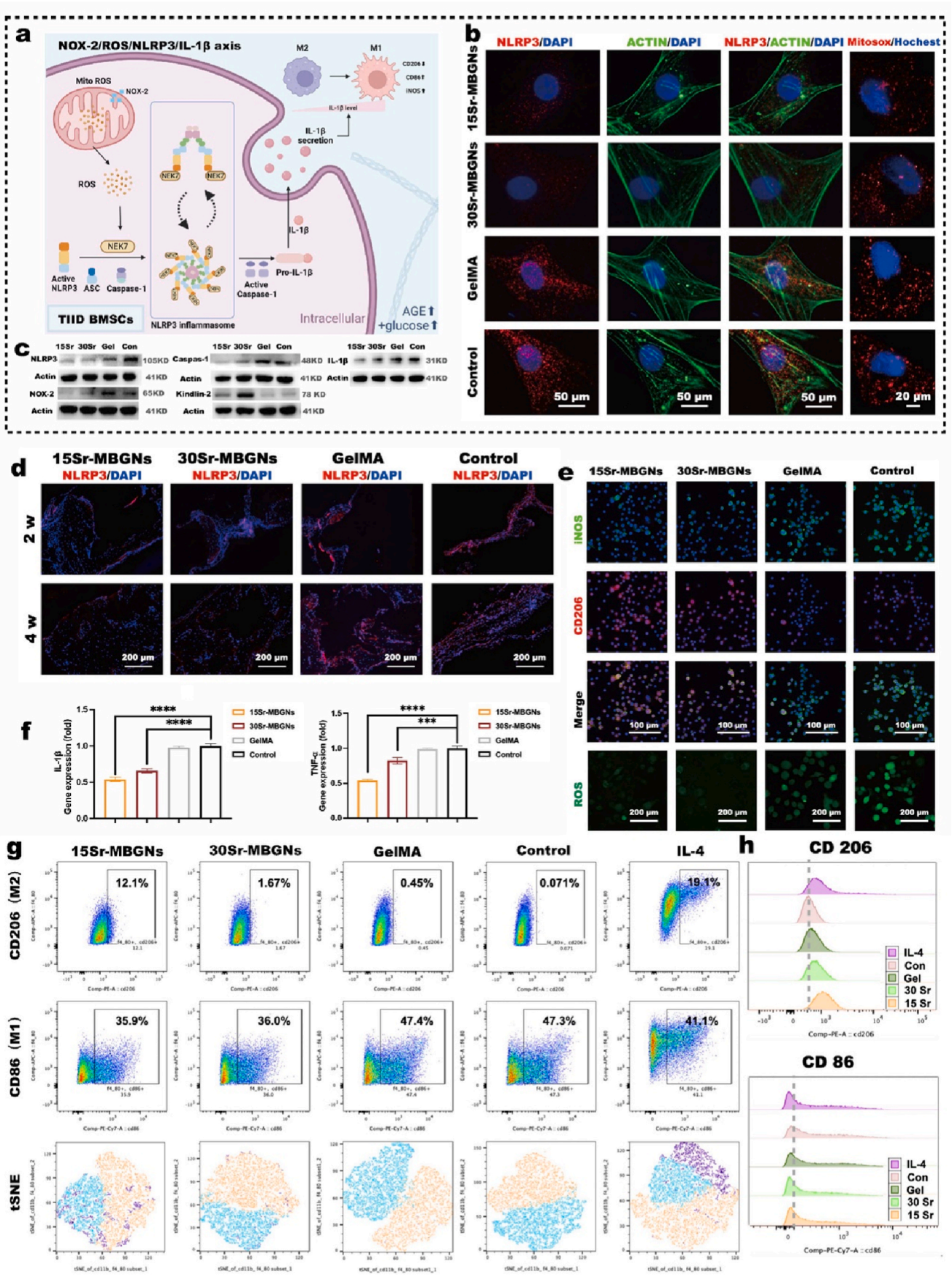

(caption on next page)

Fig. 6. Immune modulation effect of Sr-MBSG hydrogel scaffolds through the regulation of the NOX2/NLRP3/ROS/IL-1β axis. a) Schematic of the mechanism behind the immune-regulatory effect (The schematic was created with BioRender.com); b) Immunofluorescence staining of the NLRP3, Actin, and MitoSOX labeling in BMSCs incubated with different Sr-MBGNs-loaded scaffolds; c) Western blot of the NOX2/NLRP3/ROS/IL-1β axis; d) IHC indicating the high expression level of NLRP3 in the 2 w and 4 w bone defect tissue of control and GelMA groups compared with Sr-MBGNs group; e) Immunofluorescence staining of ROS and macrophage polarization markers iNOS and CD206; f) qPCR analysis of inflammatory cytokines expression in BMSCs; g-h) Analysis of macrophage polarization by flow cytometry, macrophages incubated with 15Sr-MBGNs exhibited superior anti-inflammation function and mediated stronger M2 polarization (***$p < 0.001$,****$p < 0.0001$ in a comparison of MBGNs groups with the control group).

added. After 30 min of stirring, certain amounts of calcium nitrate tetrahydrate and strontium nitrate were sequentially added to the above mixture at an interval of 30 min. The amounts of Ca and Sr precursors were determined by the nominal compositions of Sr-MBGNs. Four types of Sr-MBGNs were synthesized, which were denoted as 0Sr-MBGBs, 5Sr-MBGNs, 15Sr-MBGNs and 30Sr-MBGNs (nominal compositions in mol%: $70SiO_2$–30CaO, $70SiO_2$–25CaO–5SrO, $70SiO_2$–15CaO–15SrO, and $70SiO_2$–0CaO–30SrO, respectively). The resulting solution was stirred for an additional 4 h. The formed nanoparticles were then collected by centrifugation and washed twice with deionized water and once with ethanol (96%). The collected deposits were dried at 60 °C overnight prior to calcination at 700 °C for 3 h with a heating rate of 2 °C/min. All chemicals were purchased from Sigma-Aldrich (USA) without further purification.

4.1.2. Characterization of Sr-MBGNs

Sr-MBGNs were characterized using field emission scanning electron microscopy (FE-SEM, Auriga, Carl Zeiss) under an accelerating voltage of 3 kV. X-ray diffraction (XRD) was performed using a D8 ADVANCE X-ray diffractometer (Bruker, USA) in a 2θ range of 10–80° with Cu K radiation. In addition, all samples were dispersed in ethanol and then dropped onto low-background silicon wafers (Bruker AXS, USA). A step size of 0.014° with a dwell time of 1 s per step was applied. To analyze the detailed porous structure of Sr-MBGNs, the particles were dispersed on a Cu net and analyzed with TEM (JEM 2100F, JEOL, Japan). The Brunauer-Emmett-Teller (BET) specific surface area (SSA) and pore size distribution of 0Sr-, 5Sr-, 15Sr-, and 30Sr-MBGNs were determined by using the nitrogen sorption analysis, conducted on a Micromeritics porosimeter (ASAP2460, Micrometrics Instrument, USA).

4.1.3. 3D printing of the Sr-MBGNs-incorporated hydrogel scaffolds

Sr-MBGNs (2 mg/ml) were directly mixed 1:1 with 10% gelatin methacrylate (GelMA, EFL-GM-60) to form a final concentration of 1 mg/ml Sr-MBGNs dispersed in 5% GelMA and form the nanocomposite hydrogel as the printable ink. The printable ink was equilibrated for 30 min at 23 °C before being loaded onto the cold plate of the 3D printer (Bioscaffold3.1, GeSiM, Germany). The scaffolds were printed with the parameters of pressure, 70 kPa; temperature, 23 °C; speed, 9.5 mm/s; strand height, 0.25 mm; and strand width,0.25 mm into a size of 10 mm × 10 mm x 1.5 mm. The scaffolds were cut into a cylinder (Φ 5 mm) for in vivo cranial defect experiments. The printed scaffolds were freeze-dried and analyzed with SEM (ZEISS Gemini 300).

4.1.4. Ion release analysis of the Sr-MBGNs-incorporated hydrogel scaffolds

The 3D-printed scaffolds (10 mm × 10 mm x 1.5 mm) were incubated in high glucose DMEM (to simulate the diabetic micromilieu). The supernatant was harvested after 1 d, 3 d, 7 d, and 14 d of incubation, and the concentrations of Sr, Ca, and Si ions were characterized by ICP-OES/MS (Agilent 7800, USA). Thereafter, the cumulative curve was drawn based on the ICP data (for each group, n = 3).

4.1.5. Characterization of the biomineralization of the 3D-printed scaffolds

To investigate the biomineralization process, the 3D-printed scaffolds were incubated in DMEM (high glucose) for 14 d. Afterward, optical registration was performed to evaluate the change in appearance change of the 3D-printed scaffolds. After freezing drying (Labconco, FreeZone, Czech Rep), the transaction regions of the brittle cracked scaffolds were investigated by FE-SEM (ZEISS Gemini 300, Germany), and the chemical composition of mineralization products was characterized using energy dispersive spectrometry (EDS) analysis during SEM observation.

4.1.6. Characterization of the mechanical properties and swelling ratio

The mechanical properties of 3D-printed scaffolds (5 mm*5 mm*3 mm cubes) were characterized with a universal testing machine (HY-0230, Hengyi, China) using a speed of 0.5 mm/min, and the data were recorded until a deformation of 80% was reached. Three replicates were performed for each group, and the representative curve for each group was made using GraphPad Prism 9. Young's modulus was calculated in the initial linear region (<5%) of the strain-stress curve. Based on the breaking point of the stress-strain curve, tress strength was calculated into the bar graph. During the incubation process in high glucose DMEM, the swelling ratio was verified through a continuous weighing process of the scaffolds after incubation for 0 h 1 h, 2 h, 3 h, 4 h, 8 h, 14 h, 18 h, and 24 h for each group.

4.1.7. Characterization of the degradation rate

To understand the degradation of overall scaffolds, we performed a degradation test (in terms of weight loss of the freeze-dried scaffolds at 0d, 1d, 3d, 7d, and 14d) for the scaffolds.

4.2. In vitro evaluation of biocompatibility

4.2.1. TIID in vitro model

The BMSCs harvested from type II diabetic rats (10 w), which are described in detail below, were cultured in high glucose DMEM supplemented with 500 ng/ml LPS to simulate chronic inflammation and a high glucose environment. The second and third passages of the cells were used for further in vitro experiments.

4.2.2. Cytotoxicity and proliferation

The CCK-8 assay was performed to evaluate the cytotoxicity of extraction solutions of 0Sr-MBGNS, 5Sr-MBGNs, 15Sr-MBGNs, and 30Sr-MBGNs at the concentrations of 0.1 mg/ml, 1 mg/ml, 5 mg/ml and 10 mg/ml through incubation with TIID BMSCs seeded in 96-well plates according to the manufacturer's protocol (Yeasen, China). The proliferation effect was evaluated by CCK-8 assay at 1 d, 3 d, and 5 d after seeding TIID BMSCs on the 3D-printed scaffolds (each group, n = 3). The EDU cell proliferation kit (Ribobio, China) was used to characterize the proliferation of the cell-seeded on the 3D-print scaffolds. 3 days after cell adhesion, the green fluorescence EDU-labeled cells on the 3D printed scaffolds represent the promoted proliferation effect of 5Sr-MBGNs, 15Sr-MBGNs, and the 30Sr-MBGNs group.

4.2.3. ALP and ARS staining

After incubating TIID BMSCs with the 3D-printed scaffolds for 14 d, samples were fixed with 4% PFA for 30 min and stained with the BCIP/NBT ALP color development kit (Beyotime Biotechnology, China) following the manufacturer's protocol (n = 3).

After 21 d of osteogenic induction, the TIID BMSCs incubated with 3D-printed scaffolds were fixed with 4% PFA for 30 min, washed with PBS, and stained with 0.1% Alizarin red (Sigma) dissolved in Tris-HCl (pH 8.3) for 30 min. The mineralized nodules with calcium deposition were stained red (n = 3) and quantified at $OD_{550\ nm}$.

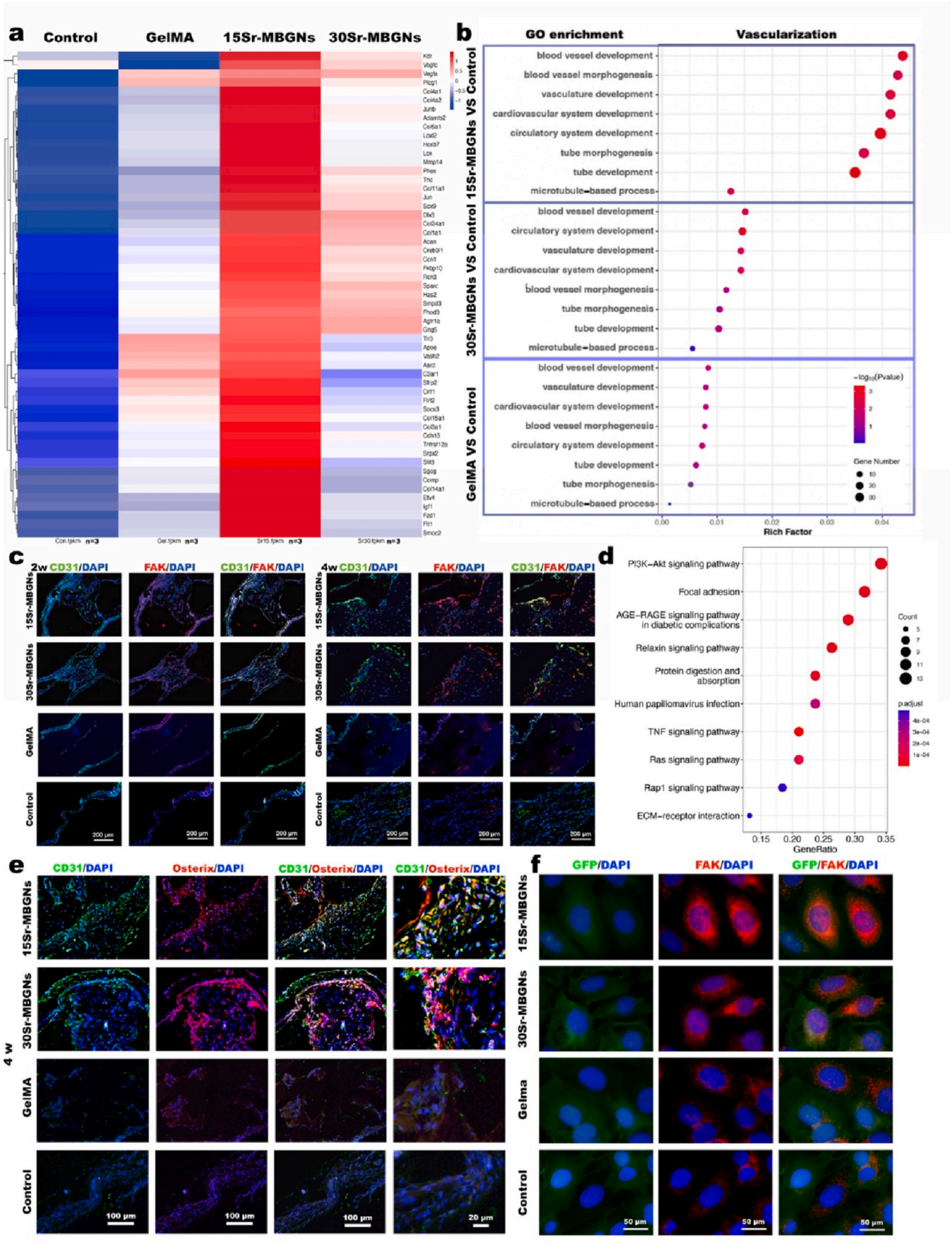

Fig. 7. Angiogenesis was enhanced by Sr-MBGNs scaffolds in a type II diabetic rat critical cranial defect model. a) Heatmap depicting the expression profile of angiogenesis genes. b) GO enrichment analysis of angiogenesis-related differentially expressed genes in the Sr-MBGNs groups in comparison with the control group. c) IHC staining of the CD31 and Fak in decalcified samples harvested at 2 w and 4 w after implantation. d) KEGG pathway analysis of Sr groups compared with the control group. e) IHC staining of the CD31 and Fak in decalcified samples harvested 4 w after implantation. f) Immunofluorescence staining of the GFP and Fak in BMSCs.

4.2.4. Real-time PCR and gene expression analysis

TIID BMSCs and Raw 264.7 cells were respectively seeded in 6-well plates and incubated with 3D-printed scaffolds for 7 d and 3d, respectively. The RNA was isolated and purified using TRIzol® reagent (Invitrogen, US) according to the manufacturer's protocol. After measuring the concentration and purity with a Thermo Scientific NanoDropTM 1000 ultraviolet–visible spectrophotometer (NanoDrop Technologies, Wilmington, DE), the RNA was reverse transcribed into cDNA using the PrimeScript RT Reagent Kit (TaKaRa, Japan). qRT-PCR was performed on the LightCyler® 480 system (Roche, Switzerland) using the SYBR Green method. The primers applied in this study were synthesized by Shenggong Co., Ltd. (Shanghai, China). The $2^{-\triangle\triangle CT}$ method was used to calculate the relative mRNA expression levels of Runx2, OCN, Col-I, Osterix, TNF-α, and IL-1β, and the housekeeping gene was used to normalize all mRNA values. GraphPad Prism (GraphPad, USA) was applied to statistically analyze the data (n = 3).

4.2.5. Western blot analysis

After culturing with the 3D-printed scaffold in high glucose DMEM (high glucose+500 ng/ml LPS) for 24 h and 7 d, TIID BMSCs seeded in 6-well plates were harvested with 100 μL RIPA lysis buffer per well (Beyotime, China). The total protein concentration was quantified with a Pierce BCA assay (Thermo Fisher Scientific, USA). 20 μg of protein from each sample was separated by 4–12%ExpressPlus PAGE (Genscript, China), followed by the transfer of samples onto a polyvinylidene fluoride (PVDF) membrane (0.2 μm, Millipore, Burlington, MA, USA). The membranes were blocked with TBST buffer containing 5% defatted milk (Beyotime, China) for 2 h at room temperature (RT) and then incubated with rabbit or mouse polyclonal primary antibodies against the following overnight at 4 °C: NLRP3, β-Actin, NOX-2, Caspase-1, Kindlin-2, IL-1β, Col-I, LOX, AGE, Fn, FAK, p-FAK, SrC, OCN, Creb1, p-Creb1, and PTH1R. Finally, the membranes were washed with PBST (0.1% Tween-20 in 0.01 M PBS), incubated with secondary antibodies (1:1000, Yeasen, China) for 1 h at RT, and then visualized with an ImageQuant LAS4000 system (GE Healthcare, Pittsburgh, PA, USA). β-Actin served as the control (n = 3).

4.2.6. Immunofluorescence staining

The harvested cells were fixed with 4% paraformaldehyde (30 min) and perforated with 0.1% Triton X-100 (15 min). The prepared samples were blocked with 5% donkey serum (Yeasen, China) for 40 min at room temperature and then incubated with the following primary antibodies overnight at 4 °C: (FAK(Rb, Abclonal, China), NLRP3 (Rb, ABMART, China), CD206 (Goat, R&D, Canada), iNOS(Rb, R&D, Canada), Kindlin-2 (Rb, ABMART, China), OPN (Rb, CST, USA), OCN (Rb, Proteintech, USA), and PTH1R (Ms, Santa Cruz, USA)). The primary antibodies were followed by fluorescently-labeled secondary antibodies (Yeasen, China) for 1 h and DAPI (Yeasen, China) for 15 min iFluor™ 488 phalloidin (Yeasen, China) was used for the staining of the cytoskeleton. The outcomes were observed using a confocal laser scanning microscope (CLSM, LEICA DMi8, Germany) platform (n = 3).

4.2.7. Detection of intracellular ROS accumulation

Intracellular ROS production was measured with an the ROS array kit (Beyotime Biotechnology, China) according to the manufacturer's instructions. Briefly, 5000 cells of Raw 264.7 cells were seeded together with the 3D-printed scaffold in the confocal dish, and 500 ng/ml LPS was added to the high glucose DMEM to simulate the inflammatory environment. 3 d later, the cells were washed with PBS and incubated with 10 μM DCFH-DA in serum-free culture medium for 30 min. Afterward, residual DCFH-DA was removed by rinsing with PBS. The images were taken by fluorescence microscopy (Scope.A1, ZEISS, Germany) at an excitation wavelength of 488 nm (n = 3).

4.2.8. Detection of mitochondrial ROS accumulation

The TIID BMSCs cultured with 3D-printed scaffolds in HG DMEM (high glucose+ 500 ng/ml) were stained with 5 μM MitoSOX Red (Invitrogen, USA) for 15 min at 37 °C to label the mitochondrial ROS. After removing the residual reacting agent, the cell nucleus were further stained with Hoechst (Yeasen, China) for 15 min. After removing the residual staining solution with Hanks (Biosharp, China), the TIID BMSCs were observed using the CLSM platform (n = 3).

4.2.9. Flow cytometry analysis

Different groups of scaffolds were incubated with M1-polarized Raw264.7 cells stimulated with LPS (500 ng/ml). The M2-polarized Raw cells stimulated with IL-4 (20 ng/ml) were used as the positive control. After 3 d, the cells were collected for flow cytometry. The group without scaffolds served as the control group. The cells were washed with PBS and labeled with FixableViabiityStain450 (BD Pharmingen, USA). After applying Fc block (CD16/CD32, BD Pharmingen, USA), the cells resuspended in staining buffer were incubated with the following antibodies: anti-CD11b FITC (BD Pharmingen), anti-F4/80 APC (eBioscience, Invitrogen, USA), and anti-CD86 PE-Cy7 (BD Pharmingen, USA). After fixation and permeation, all samples were incubated with anti-CD206 PE (eBioscience, Invitrogen, USA). The samples were tested on a BD LSRFortessa (BD, USA). The data were analyzed with FlowJo software (TreeStar Inc. USA)

4.3. In vivo analysis of the osteogenesis anti-inflammatory and angiogenic function

4.3.1. Animal model and surgical procedures

Sprague–Dawley (SD) rats were obtained from the Ninth People's Hospital Animal Center (Shanghai, China). All the in vivo experimental procedures applied in the present study were approved by the Animal Ethics Committee of the Ninth People's Hospital, Shanghai Jiao Tong University School of Medicine (SH9H-2021-A30-1).

The type II diabetic model was developed by a three-week male SD rat fed with a high-fat diet (high-fat diet with 60 kal%, FB-12492, Wuxi Fanbo Biotechnology Co., Ltd, China) for 4 w followed by a fasting injection of low-dose streptozotocin (STZ, S0130, Sigma-Aldrich, Missouri, USA) at 30 mg/kg. Successful TIIDM model construction was verified by fasting glucose levels consistently over 11.1 mmol/L for 2 w. Afterward, all rats were switched to regular diets.

Two cranial defects were carefully generated. Briefly, a scalp incision was made under general anesthesia (isoflurane, Ringpu Bio-Pharmacy Co., Ltd, Tianjin), and the cranial bone was exposed by elevating both the skin and the periosteum. Two circular critical-sized defects were formed using a 5 mm diameter trephine bur. Control groups without scaffolds and scaffolds from the three study groups (GelMA, 15Sr-MBGNs, 30Sr-MBGNs) were arranged, and the surgical sites were layer sutured. For one rat, two defects were performed.

At 2 w (n = 3), 4 w (n = 6), and 8 w (n = 6), the rats were sacrificed, and the cranial bone was harvested for further analysis.

4.3.2. Transcriptome sequencing and data processing

To investigate the mRNA expression level during the regeneration process for the cranial bone defect in the type II diabetes model, the cranial bone was harvested at 4 w (n = 3). After the periosteum and muscles were removed, the growing bone and materials in the previous bone defect region were collected. Total RNA of the bone tissue was isolated using the TRIzol® reagent (Invitrogen Life Technologies, USA) and quantified using a NanoDrop spectrophotometer (Thermo Scientific, USA).

Sequencing libraries were generated using the TruSeq RNA Sample Preparation Kit (Illumina, San Diego, CA, USA). The sequencing library was then sequenced on a HiSeq platform (Illumina) by Shanghai Personal Biotechnology Cp. Ltd. [58]..

The original data in FASTQ format (Raw Data) were filtered by Cutadapt software to obtain high-quality sequences (Clean Data) for further analysis. The reference genome index was built with Bowtie2

and the filtered reads were mapped to the reference genome "Rattus_norvegicus.Rnor_6.0.dna.toplevel.fa" (Database version: Ensembl 104.6).

HTSeq statistics were introduced to compare the read count values on each gene as the original expression of the gene, and then FPKM was used to standardize the expression. DESeq was used to analyze the differentially expressed genes of according to the following screening criteria: expression difference multiple |log2 Fold Change| > 1, and a significant P-value <0.05. Principal component analysis was performed using the prcomp function. The R package Pheatmap was used to perform bidirectional clustering analysis of all differentially expressed genes of samples. Afterward, based on the Gene Ontology database, the R package topGO was used for GO enrichment analysis of osteogenesis, angiogenesis, ions, adhesion, and biomineralization functions. The differentially expressed genes revealed in GO enrichment were collected to draw a heatmap, to illustrate the gene expression level of the same gene in different groups. Finally, by counting the number of differentially expressed genes at different levels of the KEGG pathway, the potentially related signaling pathways in which the differentially expressed genes are mainly involved were determined.

4.3.3. Sequential fluorescent labeling

Briefly, 30 mg/kg alizarin red (AR), 25 mg/kg tetracycline (TE), and 20 mg/kg calcein (CA) were injected at 2, 4, and 6 w respectively, and at 8 w the animals were euthanized to obtain the specimens (n = 3). The harvested specimens were embedded in PMMA and cut into ~150 mm thick slices, and ground and polished to a final thickness of ~40 mm. These undecalcified sections were observed for fluorescent labeling under confocal laser scanning microscopy (CLSM, LEICA DMi8, Germany). The excitation/emission wavelengths of the fluorophores were 543/617 nm (AR), 405/580 nm (TE), and 488/517 nm (CA).

4.3.4. Immunofluorescence histological staining

The specimens were harvested at the corresponding time points, which were fixed in 10% formalin for 24 h and then transferred for micro-CT (Scanco Medical MicroCT50, Switzerland) analysis before decalcification in 20% EDTA for 8 w.

The decalcified samples were embedded in paraffin, sectioned (4 μm), histologically analyzed, and immunofluorescently stained. After dewaxing, the paraffin sections were assessed by hematoxylin-eosin (H&E, Solarbio) staining and Masson trichrome staining (Solarbio) for histological analysis. Specifically, the slices were incubated with primary antibodies against CD31(1:100, CST, USA), FAK (1:50,Abclonal, China), Osrerix (1:100, Abcam, UK), Col-I (1:100, Abcam, UK), AGE (1:100,Biossantibodies, China), OPN (1:100, CST, USA), LOX (1:100, Abcam, UK), PTH1R (1:50, Santa Cruz, USA), Kindlin2 (1:50, Abmart, China), OCN (1:50, Proteintech, USA), followed by fluorescently labeled secondary antibodies (1:200, Yeasen, China) and DAPI (Yeasen, China). After observation under a fluorescence microscope, the sections were restained with HE (Solarbio, China) staining (n = 3).

4.4. Statistical analysis

All data are displayed as the mean ± standard deviation. Statistical analyses were carried out through GraphPad Prism 9 statistical software (GraphPad, USA). The normality distribution of the data was confirmed by using the Shapiro-Wilk test, while the outlier was identified by Grubbs' test. Afterward, Student's t-test or one-way analysis of variance (ANOVA) followed by Tukey's post-hoc test for multiple comparisons was used for statistical evaluation. Differences were considered significant only if the p-value was less than 0.05. *represent $p < 0.05$, **represent $p < 0.01$,***represent $p < 0.001$,**** represent $p < 0.0001$.

CRediT authorship contribution statement

Zeqian Xu: Conceptualization, Methodology, Formal analysis, Investigation, Data curation, Writing – original draft, Writing – review & editing, Funding acquisition. **Xuanyu Qi:** Formal analysis, Investigation, Data curation, Visualization, Writing – review & editing. **Minyue Bao:** Investigation, Visualization, Data curation. **Tian Zhou:** Investigation, Visualization. **Junfeng Shi:** Software, Visualization. **Zhiyan Xu:** Investigation. **Mingliang Zhou:** Validation. **Aldo R. Boccaccini:** Methodology, Resources, Writing – review & editing. **Kai Zheng:** Conceptualization, Methodology, analysis, Formal analysis, Resources, Writing – review & editing, Funding acquisition. **Xinquan Jiang:** Conceptualization, Resources, Writing – review & editing, Supervision, Funding acquisition.

Declaration of competing interest

The authors declare no conflict of interest in this study.

Acknowledgments

This work was jointly supported by the National Natural Science Foundation of China (Grant Nos. 81991505, **82130027, 81921002, 82101071,** 82270953), the Innovative research team of high-level local universities in Shanghai (SHSMU-ZLCX20212400), and the Natural Science Foundation of Jiangsu Province (No. BK20210528). The author would like to show gratitude for the support from Shanghai Postdoctoral Excellence Program (2020328). The authors gratefully acknowledge the Shanghai Institute of Precision Medicine platform for offering the support of flow cytometry.

Appendix A. Supplementary data

Supplementary data to this article can be found online at https://doi.org/10.1016/j.bioactmat.2023.01.024.

References

[1] P. Saeedi, I. Petersohn, P. Salpea, B. Malanda, S. Karuranga, N. Unwin, et al., Global and regional diabetes prevalence estimates for 2019 and projections for 2030 and 2045: results from the international diabetes federation diabetes atlas, Diabetes Res. Clin. Pract. 157 (2019), 107843.
[2] W.A. Camargo, R. de Vries, J. van Luijk, J.W. Hoekstra, E.M. Bronkhorst, J. A. Jansen, et al., Diabetes mellitus and bone regeneration: a systematic review and meta-analysis of animal studies, Tissue Eng. B Rev. 23 (5) (2017) 471–479.
[3] A. Sapra, P. Bhandari, Diabetes Mellitus. StatPearls. Treasure Island (FL), StatPearls Publishing Copyright © 2022, StatPearls Publishing LLC., 2022.
[4] A.K. Picke, G. Campbell, N. Napoli, L.C. Hofbauer, M. Rauner, Update on the impact of type 2 diabetes mellitus on bone metabolism and material properties, Endocr Connect 8 (3) (2019) R55–r70.
[5] V.D. Dixit, Nlrp3 inflammasome activation in type 2 diabetes: is it clinically relevant? Diabetes 62 (1) (2012) 22–24.
[6] A. Sharma, J.S.Y. Choi, N. Stefanovic, A. Al-Sharea, D.S. Simpson, N. Mukhamedova, et al., Specific NLRP3 inhibition protects against diabetes-associated atherosclerosis, Diabetes 70 (3) (2020) 772–787.
[7] P. de Oliveira, E.A. Bonfante, E.T.P. Bergamo, S.L.S. de Souza, L. Riella, A. Torroni, et al., Obesity/metabolic syndrome and diabetes mellitus on peri-implantitis, Trends Endocrinol. Metabol. 31 (8) (2020) 596–610.
[8] I.M. Stratton, A.I. Adler, H.A. Neil, D.R. Matthews, S.E. Manley, C.A. Cull, et al., Association of glycaemia with macrovascular and microvascular complications of type 2 diabetes (UKPDS 35): prospective observational study, BMJ 321 (7258) (2000) 405–412.
[9] P.S. Hinton, K. Shankar, L.M. Eaton, R.S. Rector, Obesity-related changes in bone structural and material properties in hyperphagic OLETF rats and protection by voluntary wheel running, Metabolism 64 (8) (2015) 905–916.
[10] N. Napoli, R. Strollo, A. Paladini, S.I. Briganti, P. Pozzilli, S. Epstein, The alliance of mesenchymal stem cells, bone, and diabetes, Internet J. Endocrinol. 2014 (2014), 690783.
[11] M.E. Locatto, H. Abranzon, D. Caferra, M.C. Fernandez, R. Alloatti, R.C. Puche, Growth and development of bone mass in untreated alloxan diabetic rats. Effects of collagen glycosylation and parathyroid activity on bone turnover, Bone Miner. 23 (2) (1993) 129–144.
[12] H. Sábado-Bundó, M. Sánchez-Garcés, C. Gay-Escoda, Bone regeneration in diabetic patients. A systematic review, Med. Oral Patol. Oral Cir. Bucal 24 (4) (2019) e425–e432.
[13] H.C. Tükel, E. Delilbaşı, Effects of metabolic syndrome on jawbones and bone metabolic markers in sucrose-fed rats, Odontology 107 (4) (2019) 457–464.

[14] M. Saito, K. Fujii, Y. Mori, K. Marumo, Role of collagen enzymatic and glycation induced cross-links as a determinant of bone quality in spontaneously diabetic WBN/Kob rats, Osteoporos. Int. 17 (10) (2006) 1514–1523.
[15] M. Retzepi, N. Donos, The effect of diabetes mellitus on osseous healing, Clin. Oral Implants Res. 21 (7) (2010) 673–681.
[16] L.M. Tilling, K. Darawil, M. Britton, Falls as a complication of diabetes mellitus in older people, J. Diabet. Complicat. 20 (3) (2006) 158–162.
[17] H. Brem, M. Tomic-Canic, Cellular and molecular basis of wound healing in diabetes, J. Clin. Invest. 117 (5) (2007) 1219–1222.
[18] J.A. de Morais, I.K. Trindade-Suedam, M.T. Pepato, E. Marcantonio Jr., A. Wenzel, G. Scaf, Effect of diabetes mellitus and insulin therapy on bone density around osseointegrated dental implants: a digital subtraction radiography study in rats, Clin. Oral Implants Res. 20 (8) (2009) 796–801.
[19] F. Javed, G.E. Romanos, Impact of diabetes mellitus and glycemic control on the osseointegration of dental implants: a systematic literature review, J. Periodontol. 80 (11) (2009) 1719–1730.
[20] C. Marcantonio, L.G. Nicoli, E. Marcantonio Junior, D.L. Zandim-Barcelos, Prevalence and possible risk factors of peri-implantitis: a concept review, J. Contemp. Dent. Pract. 16 (9) (2015) 750–757.
[21] Z. Xu, S. Han, Z. Gu, J. Wu, Advances and impact of antioxidant hydrogel in chronic wound healing, Adv Healthc Mater 9 (5) (2020), e1901502.
[22] H. Wang, Z. Xu, M. Zhao, G. Liu, J. Wu, Advances of hydrogel dressings in diabetic wounds, Biomater. Sci. 9 (5) (2021) 1530–1546.
[23] Y. Liang, M. Li, Y. Yang, L. Qiao, H. Xu, B. Guo, pH/glucose dual responsive metformin release hydrogel dressings with adhesion and self-healing via dual-dynamic bonding for athletic diabetic foot wound healing, ACS Nano 16 (2) (2022) 3194–3207.
[24] B. Li, R. Shu, W. Dai, F. Yang, H. Xu, X. Shi, et al., Bioheterojunction-engineered polyetheretherketone implants with diabetic infectious micromilieu twin-engine powered disinfection for boosted osteogenicity, Small (2022), e2203619.
[25] X. Dai, B.C. Heng, Y. Bai, F. You, X. Sun, Y. Li, et al., Restoration of electrical microenvironment enhances bone regeneration under diabetic conditions by modulating macrophage polarization, Bioact. Mater. 6 (7) (2021) 2029–2038.
[26] S.C. Tao, X.R. Li, W.J. Wei, Z.Y. Wei, C.R. Zhang, F. Wang, et al., Polymeric coating on β-TCP scaffolds provides immobilization of small extracellular vesicles with surface-functionalization and ZEB1-Loading for bone defect repair in diabetes mellitus, Biomaterials 283 (2022), 121465.
[27] X. Sun, Z. Ma, X. Zhao, W. Jin, C. Zhang, J. Ma, et al., Three-dimensional bioprinting of multicell-laden scaffolds containing bone morphogenic protein-4 for promoting M2 macrophage polarization and accelerating bone defect repair in diabetes mellitus, Bioact. Mater. 6 (3) (2021) 757–769.
[28] B. Cortet, Use of strontium as a treatment method for osteoporosis, Curr. Osteoporos. Rep. 9 (1) (2011) 25–30.
[29] L. Chen, Q. Guo, Q. Wang, C. Luo, S. Chen, S. Wen, et al., Association between plasma strontium, a bone-seeking element, and type 2 diabetes mellitus, Clin. Nutr. 39 (7) (2020) 2151–2157.
[30] C. Bizelli-Silveira, H. Pullisaar, L.A. Abildtrup, O.Z. Andersen, R. Spin-Neto, M. Foss, et al., Strontium enhances proliferation and osteogenic behavior of periodontal ligament cells in vitro, J. Periodontal. Res. 53 (6) (2018) 1020–1028.
[31] K. Zheng, W. Niu, B. Lei, A.R. Boccaccini, Immunomodulatory bioactive glasses for tissue regeneration, Acta Biomater. 133 (2021) 168–186.
[32] K. Zheng, B. Sui, K. Ilyas, A.R. Boccaccini, Porous bioactive glass micro- and nanospheres with controlled morphology: developments, properties and emerging biomedical applications, Mater. Horiz. 8 (2) (2021) 300–335.
[33] G.D. Chen, X.Y. Liang, P. Zhang, S.T. Lin, C.C. Cai, Z.Y. Yu, et al., Bioinspired 3D printing of functional materials by harnessing enzyme-induced biomineralization, Adv. Funct. Mater. 32 (34) (2022) 1–10.
[34] M. Xie, Y. Shi, C. Zhang, M. Ge, J. Zhang, Z. Chen, et al., In situ 3D bioprinting with bioconcrete bioink, Nat. Commun. 13 (1) (2022) 3597.
[35] S. Brunauer, L.S. Deming, W.E. Deming, E. Teller, On a theory of the van der Waals adsorption of gases, J. Am. Chem. Soc. 62 (7) (1940) 1723–1732.
[36] K. Zheng, J. Kang, B. Rutkowski, M. Gawęda, J. Zhang, Y. Wang, et al., Toward highly dispersed mesoporous bioactive glass nanoparticles with high Cu concentration using Cu/ascorbic acid complex as precursor, Front. Chem. 7 (2019) 497.
[37] W.C. Lepry, S.N. Nazhat, A review of phosphate and borate sol–gel glasses for biomedical applications, Adv. NanoBiomed Res. 1 (3) (2021), 2000055.
[38] K. Zheng, N. Taccardi, A.M. Beltrán, B. Sui, T. Zhou, V.R.R. Marthala, et al., Timing of calcium nitrate addition affects morphology, dispersity and composition of bioactive glass nanoparticles, RSC Adv. 6 (97) (2016) 95101–95111.
[39] H. Pan, X.Y. Liu, R. Tang, H.Y. Xu, Mystery of the transformation from amorphous calcium phosphate to hydroxyapatite, Chem. Commun. 46 (39) (2010) 7415–7417.
[40] K. Zheng, J. Wu, W. Li, D. Dippold, Y. Wan, A.R. Boccaccini, Incorporation of Cu-containing bioactive glass nanoparticles in gelatin-coated scaffolds enhances bioactivity and osteogenic activity, ACS Biomater. Sci. Eng. 4 (5) (2018) 1546–1557.
[41] R.R. Braga, Calcium phosphates as ion-releasing fillers in restorative resin-based materials, Dent. Mater. 35 (1) (2019) 3–14.
[42] M.D. Vlad, S. Gómez, M. Barracó, J. López, E. Fernández, Effect of the calcium to phosphorus ratio on the setting properties of calcium phosphate bone cements, J. Mater. Sci. Mater. Med. 23 (9) (2012) 2081–2090.
[43] F. Wu, Y. Pang, J. Liu, Swelling-strengthening hydrogels by embedding with deformable nanobarriers, Nat. Commun. 11 (1) (2020) 1–10.
[44] A.R. Boccaccini, M. Erol, W.J. Stark, D. Mohn, Z. Hong, J.F. Mano, Polymer/bioactive glass nanocomposites for biomedical applications: a review, Compos. Sci. Technol. 70 (13) (2010) 1764–1776.
[45] N. Mei, Y. Wu, B. Chen, T. Zhuang, X. Yu, B. Sui, et al., 3D-printed mesoporous bioactive glass/GelMA biomimetic scaffolds for osteogenic/cementogenic differentiation of periodontal ligament cells, Front. Bioeng. Biotechnol. 10 (2022), 950970.
[46] J. Zheng, F. Zhao, W. Zhang, Y. Mo, L. Zeng, X. Li, et al., Sequentially-crosslinked biomimetic bioactive glass/gelatin methacryloyl composites hydrogels for bone regeneration, Mater Sci Eng C Mater Biol Appl 89 (2018) 119–127.
[47] H. Ma, C. Feng, J. Chang, C. Wu, 3D-printed bioceramic scaffolds: from bone tissue engineering to tumor therapy, Acta Biomater. 79 (2018) 37–59.
[48] L. Luo, Y. He, L. Jin, Y. Zhang, F.P. Guastaldi, A.A. Albashari, et al., Application of bioactive hydrogels combined with dental pulp stem cells for the repair of large gap peripheral nerve injuries, Bioact. Mater. 6 (3) (2021) 638–654.
[49] M. Murshed, Mechanism of bone mineralization, Cold Spring Harb. Perspect. Med. 8 (12) (2018).
[50] F. Nudelman, K. Pieterse, A. George, P.H. Bomans, H. Friedrich, L.J. Brylka, et al., The role of collagen in bone apatite formation in the presence of hydroxyapatite nucleation inhibitors, Nat. Mater. 9 (12) (2010) 1004–1009.
[51] D. Kim, B. Lee, S. Thomopoulos, Y.S. Jun, The role of confined collagen geometry in decreasing nucleation energy barriers to intrafibrillar mineralization, Nat. Commun. 9 (1) (2018) 962.
[52] L. Yu, M. Wei, Biomineralization of collagen-based materials for hard tissue repair, Int. J. Mol. Sci. 22 (2) (2021).
[53] M. Saito, K. Marumo, Bone quality in diabetes, Front. Endocrinol. 4 (2013) 72.
[54] M. Saito, S. Mori, T. Mashiba, S. Komatsubara, K. Marumo, Collagen maturity, glycation induced-pentosidine, and mineralization are increased following 3-year treatment with incadronate in dogs, Osteoporos. Int. 19 (9) (2008) 1343–1354.
[55] C. Aoki, K. Uto, K. Honda, Y. Kato, H. Oda, Advanced glycation end products suppress lysyl oxidase and induce bone collagen degradation in a rat model of renal osteodystrophy, Lab. Invest. 93 (11) (2013) 1170–1183.
[56] J.G. Snedeker, A. Gautieri, The role of collagen crosslinks in ageing and diabetes - the good, the bad, and the ugly, Muscles Ligaments Tendons J. 4 (3) (2014) 303–308.
[57] X. Xiao, J. Ren, J. Chen, Z. Liu, Y. Tian, N.R. Nabar, et al., LOX-related collagen crosslink changes act as an initiator of bone fragility in a ZDF rats model, Biochem. Biophys. Res. Commun. 495 (1) (2018) 821–827.
[58] O. Saatci, A. Kaymak, U. Raza, P.G. Ersan, O. Akbulut, C.E. Banister, et al., Targeting lysyl oxidase (LOX) overcomes chemotherapy resistance in triple negative breast cancer, Nat. Commun. 11 (1) (2020) 2416.
[59] W.F. Zambuzzi, A. Bruni-Cardoso, J.M. Granjeiro, M.P. Peppelenbosch, H.F. de Carvalho, H. Aoyama, et al., On the road to understanding of the osteoblast adhesion: cytoskeleton organization is rearranged by distinct signaling pathways, J. Cell. Biochem. 108 (1) (2009) 134–144.
[60] I.V. Fadeeva, D.V. Deyneko, A.A. Forysenkova, V.A. Morozov, S.A. Akhmedova, V. A. Kirsanova, et al., Strontium substituted β-tricalcium phosphate ceramics: physiochemical properties and cytocompatibility, Molecules 27 (18) (2022) 6085.
[61] C. Fernandes, M.R. Veiga, M.T.S. Peracoli, W.F. Zambuzzi, Modulatory effects of silibinin in cell behavior during osteogenic phenotype, J. Cell. Biochem. 120 (8) (2019) 13413–13425.
[62] N. Pischon, J.M. Mäki, P. Weisshaupt, N. Heng, A.H. Palamakumbura, P. N'Guessan, et al., Lysyl oxidase (lox) gene deficiency affects osteoblastic phenotype, Calcif. Tissue Int. 85 (2) (2009) 119–126.
[63] T. Moriishi, R. Ozasa, T. Ishimoto, T. Nakano, T. Hasegawa, T. Miyazaki, et al., Osteocalcin is necessary for the alignment of apatite crystallites, but not glucose metabolism, testosterone synthesis, or muscle mass, PLoS Genet. 16 (5) (2020), e1008586.
[64] F.L. Bilotta, B. Arcidiacono, S. Messineo, M. Greco, E. Chiefari, D. Britti, et al., Insulin and osteocalcin: further evidence for a mutual cross-talk, Endocrine 59 (3) (2018) 622–632.
[65] X. Fu, B. Zhou, Q. Yan, C. Tao, L. Qin, X. Wu, et al., Kindlin-2 regulates skeletal homeostasis by modulating PTH1R in mice, Signal Transduct. Targeted Ther. 5 (1) (2020) 297.
[66] P. Lyu, B. Li, P. Li, R. Bi, C. Cui, Z. Zhao, et al., Parathyroid hormone 1 receptor signaling in dental mesenchymal stem cells: basic and clinical implications, Front. Cell Dev. Biol. 9 (2021), 654715.
[67] J. Bobek, V. Oralova, H. Lesot, A. Kratochvilova, J. Doubek, E. Matalova, Onset of calciotropic receptors during the initiation of mandibular/alveolar bone formation, Ann. Anat. 227 (2020), 151427.
[68] J. Zhan, H. Zhang, Kindlins: roles in development and cancer progression, Int. J. Biochem. Cell Biol. 98 (2018) 93–103.
[69] L. Guo, T. Cai, K. Chen, R. Wang, J. Wang, C. Cui, et al., Kindlin-2 regulates mesenchymal stem cell differentiation through control of YAP1/TAZ, J. Cell Biol. 217 (4) (2018) 1431–1451.
[70] W. Marcinkowski, G. Zhang, M. Smogorzewski, S.G. Massry, Elevation of [Ca2+]i of renal proximal tubular cells and down-regulation of mRNA of PTH-PTHrP, V1a and AT1 receptors in kidney of diabetic rats, Kidney Int. 51 6 (1997) 1950–1955.
[71] M.L. Picton, P.R. Moore, E.B. Mawer, D. Houghton, A.J. Freemont, A.J. Hutchison, et al., Down-regulation of human osteoblast PTH/PTHrP receptor mRNA in end-stage renal failure, Kidney Int. 58 (4) (2000) 1440–1449.
[72] A.P. Liu, E.A. Appel, P.D. Ashby, B.M. Baker, E. Franco, L. Gu, et al., The living interface between synthetic biology and biomaterial design, Nat. Mater. 21 (4) (2022) 390–397.
[73] J. Yan, G. Tie, S. Wang, A. Tutto, N. DeMarco, L. Khair, et al., Diabetes impairs wound healing by Dnmt1-dependent dysregulation of hematopoietic stem cells differentiation towards macrophages, Nat. Commun. 9 (1) (2018) 33.

[74] Y. Sun, Q. Zhou, Y. Du, J. Sun, W. Bi, W. Liu, et al., Dual biosignal-functional injectable microspheres for remodeling osteogenic microenvironment, Small 18 (36) (2022), e2201656.
[75] P.D. Sarkar, A.B. Choudhury, Relationships between serum osteocalcin levels versus blood glucose, insulin resistance and markers of systemic inflammation in central Indian type 2 diabetic patients, Eur. Rev. Med. Pharmacol. Sci. 17 (12) (2013) 1631–1635.
[76] S. Chen, X. Wu, Y. Lai, D. Chen, X. Bai, S. Liu, et al., Kindlin-2 inhibits Nlrp3 inflammasome activation in nucleus pulposus to maintain homeostasis of the intervertebral disc, Bone Res. 10 (1) (2022) 5.
[77] K.H. Yiu, H.F. Tse, Specific role of impaired glucose metabolism and diabetes mellitus in endothelial progenitor cell characteristics and function, Arterioscler. Thromb. Vasc. Biol. 34 (6) (2014) 1136–1143.
[78] X. Zhao, J.L. Guan, Focal adhesion kinase and its signaling pathways in cell migration and angiogenesis, Adv. Drug Deliv. Rev. 63 (8) (2011) 610–615.
[79] J. Filipowska, K.A. Tomaszewski, Ł. Niedźwiedzki, J.A. Walocha, T. Niedźwiedzki, The role of vasculature in bone development, regeneration and proper systemic functioning, Angiogenesis 20 (3) (2017) 291–302.
[80] K. Zheng, E. Torre, A. Bari, N. Taccardi, C. Cassinelli, M. Morra, et al., Antioxidant mesoporous Ce-doped bioactive glass nanoparticles with anti-inflammatory and pro-osteogenic activities, Mater. Today Bio. 5 (2020), 100041.